Acta Pharmaceutica Sinica B 2026;16(2):1116−1139

Chinese Pharmaceutical Association
Institute of Materia Medica, Chinese Academy of Medical Sciences

Acta Pharmaceutica Sinica B

www.elsevier.com/locate/apsb
www.sciencedirect.com

ORIGINAL ARTICLE

A systemic immunogenic reactor leveraging modified γ-cyclodextrins for photo-controlled cancer Ca^{2+} interference *via* modulating MICU1

Qian Jing[†], Mengnan Zhao[†], Yan Tang, Tao Chen, Mingyan Sun, Dandan Mi, Lan Zou, Rujing Wang, Jun Lu[*], Sanjun Shi[*]

State Key Laboratory of Southwestern Chinese Medicine Resources, Lab for Innovation & Effective Uses of Chinese Drug Germplasm Resources, School of Pharmacy, College of Modern Chinese Medicine Industry, Chengdu University of Traditional Chinese Medicine, Chengdu 611137, China

Received 4 March 2025; received in revised form 23 June 2025; accepted 10 August 2025

KEY WORDS

Ca doping cyclodextrin;
Metal-organic frameworks;
Hypericin;
pH-sensitive;
Photo-controlled mitochondrial calcium overload;
MICU1;
Pyroptosis;
Immunotherapy

Abstract Interference with calcium homeostasis provokes tumor cell death and immune response, providing a novel direction for tumor immunotherapy as a promising cancer treatment strategy. Nevertheless, most reported Ca^{2+}-overloaded nanoinducers encounter challenges such as intricate preparation procedures, safety concerns arising from inorganic material input, and limited anti-tumor efficiency. Herein, we synthesized a biocompatible and pH-sensitive Ca-doped cyclodextrin metal-organic framework (Ca/K-MOF) as a carrier, which was then loaded with photosensitizer hypericin (HY) *via* a simple one-pot synthesis to form HY@Ca/K-MOF. To enhance the stability both *in vitro* and *in vivo*, we coated HY@Ca/K-MOF with a hydrophilic layer of PEG (^{PEG}HY@Ca/K-MOF). When exposed to 590 nm photoirradiation, ^{PEG}HY@Ca/K-MOF, with its pH-responsive dissociation, the Ca^{2+} and HY mediators released at the tumor site share the responsibility of triggering intracellular Ca^{2+} disturbances, which amplified the production of reactive oxygen species (ROS) and led to mitochondrial calcium overload through modulating mitochondrial MICU1 function. Under photocontrol, this interplay between ROS generation and mitochondrial calcium overload created a bidirectional amplification effect, where each process reinforced the other, subsequently eliciting a pyroptosis-evoked immune response. Significantly, this newly constructed delivery platform effectively suppressed both primary and distant tumors without

*Corresponding authors.
E-mail addresses: shisanjuns@163.com, shisanjuns@cdutcm.edu.cn (Sanjun Shi), ljaaa111@163.com (Jun Lu).
[†]These authors made equal contributions to this work.

Peer review under the responsibility of Chinese Pharmaceutical Association and Institute of Materia Medica, Chinese Academy of Medical Sciences.

https://doi.org/10.1016/j.apsb.2025.10.046

the need for additional immunological interventions. In summary, this Ca^{2+}-doped MOF-based nanomaterial provides a promising approach for efficient tumor photo-controlled mitochondrial Ca^{2+} overload-pyroptosis immunotherapy.

1. Introduction

Metal-organic frameworks (MOFs), also known as crystalline porous hybrid materials, are composed of fundamental inorganic and organic building blocks that self-assemble. A critical factor impeding their application in cancer therapy is their biosafety; the release of metal ions and organic ligands from decomposing MOFs poses potential biosafety hazards in biological systems[1-3]. Undoubtedly, it is imperative to identify MOFs that are low or non-toxic and composed of biocompatible ligands and metal ions before they can be widely used in the clinic. To this end, incorporating natural organic ligands and low molecular weight metal centers can significantly enhance the biocompatibility of these materials. γ-Cyclodextrin metal-organic frameworks (γ-CD-MOFs) are a novel class of materials that combine the biocompatibility of cyclodextrins with the porous structure of metal-organic frameworks (MOFs). Cyclodextrins are naturally occurring carbohydrates known for their renewability, non-toxicity, and edibility[4,5]. CD-MOF materials feature high specific surface areas, tunable porosity, superior biocompatibility and biodegradability, positioning them as promising candidates for applications in the biomedical, agricultural, and food industries[6,7]. Importantly, the European Drug Administration (EMA) and the US Food and Drug Administration (FDA) have approved natural cyclodextrins and their derivatives as safe additives[8]. Traditional MOFs, composed of aromatic polyacids and polybases, often pose challenges for medical applications[9-12]. In contrast, CD-MOFs primarily use γ-cyclodextrin as the organic ligand and potassium ions as the metal center, demonstrating excellent biosafety and medicinal value[13]. Hence, cyclodextrin-based organic oligomer delivery carriers represent a novel, safe pharmaceutical excipient.

However, the metal center of CD-MOFs, being potassium ions (K^+), exhibits relatively low stability and bioactivity, which limits the development of drug carriers based on this platform. Doping in biomaterials involves introducing other elements or compounds to enhance their properties or impart new functionalities, thereby improving their mechanical, chemical, and biological performance[14]. For instance, europium ions, characterized by their f-f intra-orbital electronic transitions, endow the doped nanoparticles with distinctive photoluminescent properties, making them highly valuable for applications in biological imaging[15]. It is well established that calcium ions (Ca^{2+}) stand as one of the most abundant metallic elements in the human body, orchestrating a plethora of vital cellular functions, including cell proliferation, differentiation, apoptosis, and the transmission of nerve impulses[16]. Therefore, the potential of doping Ca^{2+} into CD-MOFs (K-MOFs) to enhance their performance, particularly in terms of drug delivery efficiency and bioactivity, is a compelling avenue for further investigation. In light of this, we discovered that Ca^{2+} release from doped CD-MOFs (Ca/K-MOFs) is pH-dependent, with no release occurring at blood pH levels compared to non-doped CD-MOFs. Besides, we also observed that Ca^{2+}-doped MOFs can disrupt intracellular Ca^{2+} concentrations and lead to calcium overload, an effective means of affecting mitochondrial dysfunction and ultimately triggering cancer cell death by increasing mitochondrial Ca^{2+} concentration[17]. However, this exogenous calcium carrier alone cannot meet the requirement for rapid calcium overload, and its capacity to generate calcium overload is restricted by the dynamic control of calcium signaling *in vivo*[18]. In this scenario, inspired by the possible crosstalk between ROS and calcium signaling in tumor cells[19], we propose that the combination of exogenous calcium ion input with photosensitizers that can produce cytotoxic singlet oxygen ($^1O_2$) might break this deadlock.

In this study, we dressed the old MOFs with new clothes and developed the inaugural Ca^{2+}-doped γ-CD-MOFs (Ca/K-MOFs), with the capability for modulation of Ca^{2+} interference. Doping significantly enhanced their bioactivity, enabling responsive Ca^{2+} release in the acidic tumor microenvironment (TME). This release induced Ca^{2+} aggregation within tumor cells, which in turn led to an increase in reactive oxygen species (ROS). Additionally, Ca/K-MOFs also exhibited excellent drug-loading capabilities. Encapsulating the photosensitizer hypericin (HY) within the cubic cavities of Ca/K-MOFs and surface-PEGylation with DSPE-$mPEG_{2000}$ yielded ^{PEG}HY@Ca/K-MOFs, not only exhibiting desirable stability and excellent pH-sensitive dissociation behavior but also boasting elevated photodynamic characteristics and a remarkable ability of light-controlled mitochondrial calcium overload. Under 590 nm irradiation, ^{PEG}HY@Ca/K-MOFs significantly produced $^1O_2$, amplifying oxidative stress and disrupting intracellular Ca^{2+} homeostasis. This light-induced mechanism disrupted mitochondrial calcium uptake 1 (MICU1) function, channeling excessive influx of Ca^{2+} into mitochondria, exacerbating severe mitochondrial damage, activating intense pyroptosis, and releasing a substantial amount of DAMPs, thereby eliciting remarkable antitumor immune responses and inhibiting the growth of both primary and distant tumors. We termed this mechanism "photo-controlled mitochondrial calcium overload-pyroptosis immunotherapy". Overall, ^{PEG}HY@Ca/K-MOF, as a newly developed initiator of photo-controlled mitochondrial calcium overload, significantly enhances the antitumor and abscopal effects, underscoring their potential in the realm of photo-controlled mitochondrial Ca^{2+} overload-pyroptosis-based tumor immunotherapy.

2. Materials and methods

2.1. Materials

Hypericin (≥95%, HY) was purchased from Guangzhou Shuntong Pharmaceutical Technology Co., Ltd. (Guangzhou, China). Methanol, ethanol, dimethylsulfoxide, polyethylene glycol 20,000 ($PEG_{20,000}$), calcium chloride ($CaCl_2$), and Tween-20 were

purchased from Chengdu Kelong Chemical Co., Ltd. (Chengdu, China). γ-Cyclodextrin (γ-CD, ≥98%) and 1,2-distearoyl-*sn*-glycero-3-phosphoethanolamine-*N*-[methoxy(polyethylene glycol)-2000] (DSPE-mPEG$_{2000}$) were obtained from Adamas (Shanghai, China). Potassium hydroxide (KOH, 90%) was purchased from Shanghai Boer Chemical Reagent Co., Ltd. (Shanghai, China). 1,3-Diphenylisobenzofuran (DPBF) and methyl thiazolyl tetrazolium (MTT) were purchased from Shanghai Yien Chemical Technology Co., Ltd. (Shanghai, China). Calcium Assay Kit and Potassium Assay Kit were purchased from Nanjing Jiancheng Bioengineering Institute (Nanjing, China). 4′,6-Diamidino-2-phenylindole dihydrochloride (DAPI), coumarin 6,2′,7′-dichlorodihydrofluorescein diacetate (DCFH-DA), and Super ECL Plus kit were purchased from Shanghai Bioscience Co., Ltd. (Shanghai, China). Ascorbic acid (VC) and menadione (VK) were purchased from Dalian Meilun Biotechnology Co., Ltd. (Dalian, China). R837 (Imiquimod), Tetrakis (acetoxymethyl)1,2-bis(2-aminophenoxy)ethane-*N*,*N*,*N*′,*N*′-tetraacetat (BAPTA-AM), MCU-i4 and DS16570511 were purchased from Aladdin (Shanghai, China). Hank's Buffered Saline (HBSS), Pluronic® F-127, Fluo-3 AM, Rhod-2 AM, Rhodamine 123 (Rh123) fluorescence probe, and Annexin V-FITC/PI apoptosis detection kit were obtained from Yeasen (Shanghai, China). Radio immunoprecipitation assay (RIPA) buffer, ATP assay kit, LDH assay kit, and Cell Mitochondria Isolation Kit were acquired from Beyotime (Shanghai, China). Permeabilization Buffer (10 ×) was purchased from Biosharp (Beijing, China). Protein-free rapid blocking solution, 0.25% Trypsin (without EDTA) solution, Triton X-100, Phosphate-buffered saline (PBS), and optimal cutting temperature compound (OCT) were purchased from Servicebio (Wuhan, China). Collagenase IV was purchased from Biofroxx (Germany). Hyaluronidase was purchased from Solarbio (Beijing, China). Polyacrylamide gel electrophoresis (SDS-PAGE) fast preparation kit, multicolor prestained protein marker, and omni-easy™ protein sample loading buffer were ordered from Epizyme (Shanghai, China). RBC Lysis Buffer, Trypsin-EDTA Solution (0.25%) and antibiotics (100 U/mL of penicillin and streptomycin) were purchased from Boster (Wuhan, China). Fetal bovine serum (FBS) was purchased from Tianhang Biotechnology Co., Ltd. (Huzhou, China). Roswell Park Memorial Institute 1640 Medium (RPMI-1640) was purchased from Corning (NY, USA). The primer sequences were synthesized by Sangon Biotech Co., Ltd. (Shanghai, China). SteadyPure Quick RNA Extraction Kit, Evo M-MLV RT Mix Kit with gDNA Clean for qPCR, and SYBR Green Premix Pro Taq HS qPCR kit were purchased from Aikerui Biotechnology Co., Ltd. (Changsha, China). The yellow LED lamp (570−590 nm) was purchased from Aijia Electric Technology Co., Ltd. (Xuzhou, China).

2.2. Synthesis of Ca/K-MOFs

K-MOF was synthesized following a previously reported method[20]. The synthesis process for Ca-doped MOFs with varying doping ratios is fundamentally identical, with the only difference being the quantities of calcium and potassium hydroxide added (Supporting Information Table S1). The preparation of Ca/K-MOF identified after screening is described below: $CaCl_2$ (0.024 g), KOH (0.08 g), and γ-CD (0.259 g) were dispersed in 8 mL of deionized water. After the mixture was sonicated in a water bath to ensure dissolution and then stirred at 50 °C for 30 min, it was then filtered through a 0.8 μm hydrophilic filter membrane. The filtrate was combined with 5 mL of methanol in a sealed container, to which 13 mL of a methanolic solution of $PEG_{20,000}$ (8 mg/mL) was added. The mixture was magnetically stirred in an ice water bath for 12 h. The white precipitates were collected through centrifugation and washed with ethanol 3 times. The Ca/K-MOFs were then isolated by centrifugation, and the solid powder obtained was dried for subsequent applications.

2.3. Preparation of HY@Ca/K-MOFs and ^{PEG}HY@Ca/K-MOFs

Firstly, the preparation of HY@Ca/K-MOF was carried out by adding 30 mg Ca/K-MOF to the HY ethanol solution (3 mL, 2 mg/mL) in a brown sample bottle and stirring at room temperature for a duration of 12 h. Afterward, the resulting suspension was separated, and the remaining drugs were washed away with ethanol to obtain HY@Ca/K-MOF. Finally, the obtained HY@Ca/K-MOF was placed in an oven to dry. Similarly, HY@K-MOF was synthesized using K-MOF (6 mg).

To obtain the PEGylated HY@Ca/K-MOF, 2 mg HY@Ca/K-MOF was dissolved in 2 mL of deionized water. Then, 2 mg DSPE-mPEG$_{2000}$ was added to continue stirring vigorously in the dark for 6 h. The final solution obtained was named ^{PEG}HY@Ca/K-MOF.

2.4. Theoretical calculations

Density functional theory (DFT) calculations were performed using the VASP software package. The exchange-correlation interactions were treated with the Perdew-Burke-Ernzerhof (PBE) functional within the generalized gradient approximation (GGA) framework. The electronic structure was described using the projected augmented wave (PAW) pseudopotential with a kinetic energy cut-off of 500 eV for the expansion of the electronic eigenfunctions. The Brillouin-zone integration was conducted using a Γ-centered 5 × 5 × 5 Monkhorst−Pack k-point mesh. The atomic positions were fully optimized until the energy and force reached a tolerance of 1×10^{-5} eV and 0.03 eV/Å, respectively. To account for the long-range interactions, the dispersion-corrected DFT-D method was implemented.

2.5. $^1O_2$ generation assessment

Singlet oxygen generation was tracked by the chemical oxidation of DPBF. DPBF can engage in an irreversible reaction with singlet oxygen, leading to a notable reduction in its absorption at 415 nm. 20 mL mixed solution containing 0.001% Tween 20, 0.25 μg/mL HY or HY-loaded MOF, and 0.05 μg/mL DPBF. Afterward, the mixture was exposed to a 590 nm yellow LED (20 mW/cm^2) at room temperature at various times. The degradation curve of DPBF was recorded by a UV−vis spectrometer. The $^1O_2$ generation rate was determined from the reduced absorbance over time.

2.6. Release performance of the HY in HY-loaded MOFs

The release profile of HY was detected by HPLC. The HY-loaded MOFs and Free HY suspensions (3 mL, 0.3 mg/mL equivalent of HY concentration) were placed in dialysis bags (MWCO = 8000−14,000). These dialysis bags were then sealed and immersed in 15 mL of release media (PBS with 0.5% Tween-20 at pH levels of 7.4, 6.5, and 5.0) to simulate different biological environments. The degradation and release experiments were carried out at 37 °C under constant shaking. For HY release, at each time interval, 1 mL of media was taken from the solution

outside the bags to measure the concentrations of HY, and 1 mL of fresh media with the same pH value was added to the solution.

2.7. *In vitro Ca^{2+} release from different Ca-doped MOFs*

To further investigate the release behavior of Ca ions at varying pH levels, Ca-doped MOFs were dissolved in NaH_2PO_4/Na_2HPO_4 media solutions adjusted to pH 7.4, 6.5, and 5.0 within a constant-temperature oscillation incubator. After a 12-h period of incubation under constant temperature and oscillation, the samples were centrifuged to separate and collect the supernatant for analysis. The contents of Ca^{2+} in the supernatant were measured by a calcium assay kit. The same procedures were used to measure the release of K^+ from the solution, and then the amount of K^+ in the supernatant was determined by a potassium assay kit.

2.8. *Assessment of intracellular Ca^{2+}*

2.8.1. *Visualization of intracellular calcium flow*

B16F10 cells were seeded in a 6-well cell plate and allowed to settle for 12 h before being subjected to different treatments for a period of 6 h. For the non-light irradiating groups, the cells were straightforwardly incubated for a full 6 h. In the light-irradiating groups, following a 4-h treatment, the cells were then exposed to 590 nm light (20 mW/cm^2, 5 min), after which they were returned to the incubator for an additional 2 h. After treatment, cells were washed with HBSS buffer, and intracellular Ca^{2+} levels were visualized using the Fluo-3 AM fluorescence probe for 1 h. Subsequently, the distribution of Ca ions in the cells was analyzed by CLSM and FCM.

2.8.2. *Mitochondrial Ca^{2+} production*

B16F10 cells were seeded in 150 mm tissue culture dishes and grown until they reached approximately 70% confluence. At this point, the cells were treated with different samples for 6 h: control, K-MOF, Ca/K-MOF, Free HY + L, HY@K-MOF + L, HY@Ca/K-MOF + L, and ^{PEG}HY@Ca/K-MOF + L. After the indicated treatment, a cell mitochondria isolation kit was used to isolate the mitochondria following the manufacturer's instructions. Afterward, the isolated mitochondria were resuspended in HBSS buffer, and the Ca^{2+} content in the mitochondria was measured with the commercial calcium assay kit. In particular, the culture medium after being treated with control or Free HY was also collected by centrifugation (13,000 rpm, 15 min) and determined by a calcium assay kit. To observe the distribution of Ca^{2+} in mitochondria after treatment with K-MOF or Ca/K-MOF, a Rhod-2 AM probe (4 μmol/L) with red fluorescence was incubated for 1 h to label mitochondrial Ca^{2+}. Images were recorded with CLSM.

2.9. *Intracellular ROS generation*

The intracellular level of ROS was detected using the ROS-sensitive fluorescence probe DCFH-DA. Following a 6-h incubation period, the treated cells were rinsed with PBS and then incubated with a 10 μmol/L diluted DCFH-DA working solution at 37 °C for 1 h. Subsequently, the cells were stained with DAPI for 5 min in the dark, and the fluorescence was examined using CLSM. In addition, the treated cells were harvested by trypsinization, resuspended in PBS, and their ROS levels were immediately detected by FCM at the excitation wavelength of 488 nm.

To elucidate the link between calcium overload and ROS, we intervened in the cells with the calcium chelator BAPTA-AM and ROS inhibitors. More specifically, after aspirating the culture medium, the cells were pre-treated with BAPTA-AM (10 μmol/L, 1 h) or VC (0.5 mmol/L, 0.5 h). Following this pre-incubation, B16F10 cells were exposed to HY@Ca/K-MOF and ^{PEG}HY@Ca/K-MOF under light conditions for a duration of 4 h. Subsequently, the cells were irradiated with a yellow 590 nm LED light at an intensity of 20 mW/cm^2 for 5 min. After an additional 2-h incubation, cells were detected by CLSM and FCM.

2.10. *Measurement of mitochondrial membrane potential*

To monitor the alterations in the intracellular mitochondrial membrane potential within the cells, we utilized Rh123 staining. After completing the aforementioned incubation and washing procedures, the cells were dyed with Rh123 (1 μmol/L) for 20 min, and changes in mitochondrial membrane potential were measured by CLSM and FCM.

2.11. *Bio-TEM observation*

B16F10 cells were seeded into 12-well plates and allowed to grow for 12 h. Cells were treated with different groups, including HY@K-MOF + L, HY@Ca/K-MOF + L, and ^{PEG}HY@Ca/K-MOF + L, at a final concentration of 32 ng/mL. After 6 h of treatment, the treated cells were prefixed with 3% glutaraldehyde, then the tissue was postfixed in 1% osmium tetroxide for 1 h at room temperature, dehydrated in a series of acetone, infiltrated in Epox 812 for a longer time, and embedded. The semithin sections were stained with methylene blue, and the ultrathin sections were cut with a diamond knife and stained with uranyl acetate and lead citrate. The prepared sections were observed with Bio-TEM.

2.12. *In vivo antitumor efficacy evaluation*

All animal experimental procedures were strictly followed the guidelines provided by the Experimental Animal Management and Ethics Committee of Chengdu University of TCM. After the tumor size reached ~50 mm^3, the melanoma-bearing C57BL/6 mice ($n = 5$) were administered PBS, Free HY, HY@K-MOF, Ca/K-MOF, HY@Ca/K-MOF, ^{PEG}HY@Ca/K-MOF, and ^{PEG}HY@Ca/K-MOF + L (equivalence dose of 15 mg/kg HY) *via* the tail vein on Days 1, 3, 5, 7, and 590 nm yellow LED irradiation was exposed to the tumor growth site of mice (20 mW/cm^2 for 5 min) in ^{PEG}HY@Ca/K-MOF + L after 12 h injection. Throughout the experimental period, the tumor volume and body weight of the mice were closely monitored on a daily basis. Tumor dimensions were measured, and volumes (V_t) were calculated as shown in Eq. (1).

$$V_t = \text{Width}^2 \times \text{Length} \times 0.5 \quad (1)$$

Following a 10-day treatment period, all mice were euthanized. Blood samples were collected for biochemical analysis, and the major organs, including the heart, liver, spleen, lung, and kidney, were harvested and fixed in 4% paraformaldehyde for subsequent H&E staining. For immunological assessment, tumor-draining lymph nodes (TDLNs), spleen, and a small proportion of tumors were collected and processed for FCM. The remaining fresh tumor tissues were prepared using three distinct methods: (1) soaked in

4% paraformaldehyde overnight and prepared for H&E and IHC use. (2) OCT embedded and then frozen at −80 °C. Subsequently, it was used for immunofluorescence staining analyses. (3) For pyroptosis evaluation *in vivo*, tumors were collected, and 100 mg of tumor tissue was clipped in every group and added to a mixture of RIPA lysate and PMSF, which was subsequently ground using a cryo-miller, placed on ice for 30 min, and centrifuged to remove the supernatant (12,000 rpm, 15 min). Pyroptosis pathway proteins were evaluated by WB analysis.

2.13. *In vivo antitumor therapy in a bilateral tumor model*

A bilateral tumor model was established to verify the potential of ^{PEG}HY@Ca/K-MOF + L to activate the systemic immune system. Female C57BL/6 mice, aged 6 to 8 weeks, were subcutaneously inoculated with 5×10^5 B16F10 cells on their right flank to form the primary tumor, and 4 days later, 3×10^5 B16F10 cells were injected into the left flank to induce a distant tumor. Once the volume of right tumor volume approached approximately 50 mm^3, mice were randomly allocated into four groups: (1) PBS (intravenous injection); (2) R837 (15 mg/kg, intratumoral injection); (3) ^{PEG}HY@Ca/K-MOF (15 mg/kg, intravenous injection); and (4) ^{PEG}HY@Ca/K-MOF (15 mg/kg, intravenous injection) followed by irradiation. For the phototherapy groups, only the primary tumor was irradiated with a 590 nm laser (20 mW/cm^2) for 5 min at 12 h post-injection, with no intervention on the distant tumor. The growth of both tumors and changes in body weight for each mouse were monitored every day. At the endpoint, anticoagulated peripheral blood, spleens, TDLNs, and tumors were surgically harvested.

To systematically investigate the immune response, mice were euthanized after receiving various treatments, and their primary tumors, distant tumors, TDLNs, and spleens were harvested for preparation of a single-cell suspension according to standard protocols. In brief, tumors were minced into tiny pieces and digested with 1 mL enzyme cocktail (collagenase type IV 0.6 mg/mL, hyaluronidase 0.1 mg/mL, and DNAase 0.02 mg/mL) at 37 °C for 1 h. Thereafter, the mixture was gently ground and filtered through a 70 μm cell strainer to obtain a single-cell suspension. TDLNs were treated similarly but incubated for 2 h before being homogenized into single-cell suspensions. Spleens were placed in 1 × PBS and gently minced with a syringe plunger, then filtered through a 70 μm cell strainer. Anticoagulated peripheral blood was centrifuged at 2000 rpm for 5 min, lysed with RBC lysis buffer for 3 min, and erythrocytes were removed from the single-cell suspensions by repeated washing with PBS. After staining with varying fluorescence-labeled antibodies, the percentages of maturated DCs ($CD80^+CD86^+$ gated on $CD11c^+$ DCs), total $CD4^+$ T cells, $CD8^+$ T cells ($CD4^+CD8^+$ gated on $CD3^+$ T cells), T_{EM} cells ($CD44^+CD62L^-$ gated on $CD8^+$ T cells), T_{CM} cells ($CD44^+CD62L^+$ gated on $CD8^+$ T cells), and Tregs ($CD25^+Foxp3^+$ gated on $CD4^+$ T cells) were analyzed using flow cytometry. FlowJo software (version 10.8.1) was used to analyze the relative percentages of these different immune cell subsets.

For immunofluorescence staining of tumor tissues, samples were rapidly embedded in the OCT compound and frozen. The frozen blocks were then sectioned using a cryotome, and the resulting slices were mounted onto slides, which were incubated with primary antibodies specific to the proteins of interest for 12 h at 4 °C. After adding fluorescently labeled secondary antibodies and staining with DAPI for 30 min, the slides were then observed using CLSM.

2.14. *Statistical analysis*

All results are expressed as mean ± standard deviation (SD), and data analyses were conducted using GraphPad Prism 8.0 software. To assess the differences between two experimental groups, a one-way analysis of variance (ANOVA) followed by Student's *t*-test (two-tailed) was employed, and differences between multiple groups were determined using a two-way ANOVA with Tukey's post-test. The P value was denoted with * for $P < 0.05$, ** for $P < 0.01$, *** for $P < 0.001$, or **** for $P < 0.0001$.

3. Results and discussion

3.1. *Ca-doped CD-MOF emerging as a potential candidate for enhanced acid responsiveness and bioactivity*

The synthesis of Ca/K-MOF and its application in cancer treatment are shown in Scheme 1. Starting from the reported γ-CD-MOF (K-MOF)[20], we modified the synthesis protocol to incorporate calcium doping. Specifically, potassium hydroxide and calcium chloride were co-crystallized with γ-CD in an aqueous methanol solution to produce partially calcium-doped CD-MOF. Six different doping levels were synthesized by varying the molar ratio of $CaCl_2$ to KOH (Table S1). The morphology and microstructure of the resulting Ca-doped MOFs were then analyzed by scanning electron microscopy (SEM). As shown in Fig. 1A, the doped MOF ($Ca_{0.2}/K_{1.4}$-MOF) synthesized with a $CaCl_2$/KOH molar ratio of 1:7 maintained the structural integrity of the original K-MOF. When the Ca content exceeds 12.5% (Ca:K = 1:7), the structure of the MOF is disrupted, and the morphology of Ca-doped MOFs turns to particles with irregular shapes. This happens most definitely due to the introduction of superfluous ligand (Ca^{2+}), which affects the crystallization process.

Based on the above SEM results, we chose Ca-doped MOFs featuring three different doping levels (4.2%, 8.3%, and 12.5%) for further analysis. All density functional theory (DFT) calculations were conducted using the Vienna Ab initio Simulation Package (VASP)[21-24]. Three doping levels of MOFs were determined based on the crystallographic information file (CIF) of γ-CD-MOF, and subsequently, the corresponding optimized geometric structures were derived (Fig. 1B). It is anticipated that the Ca heteroatom contributes to the rearrangement of electron distribution on the surface. Fig. 1C reveals that the electronic structure of the metal center was modulated after the doping of Ca. Specifically, a reduction in charge density at the K site corresponded with an increase around O and C atoms adjacent to Ca, indicative of charge transfer processes from K to Ca. To explore the electronic coupling and orbital contributions, we calculated the band structure and density of states (DOS) for both K-MOF and Ca-doped MOFs. The Fermi energy level, corresponding to the highest occupied orbital, was referenced at 0 eV. The bandgap was observed to narrow from 2.61 to 1.86 eV with escalating Ca doping concentration (Fig. 1D). That is, introducing a higher concentration of Ca dopants into the MOF at levels below 12.5% can give rise to a downward shift in the conduction band edge (E_{CB}), leading to a net electronic bandgap-narrowing effect. This leads to a denser energy band profile and the creation of localized charge distributions, facilitating electron transitions across the band gap. The enhancement of the charge exchange region indicates that the doped Ca possesses abundant electron exchange with its coordination environment, thereby improving the

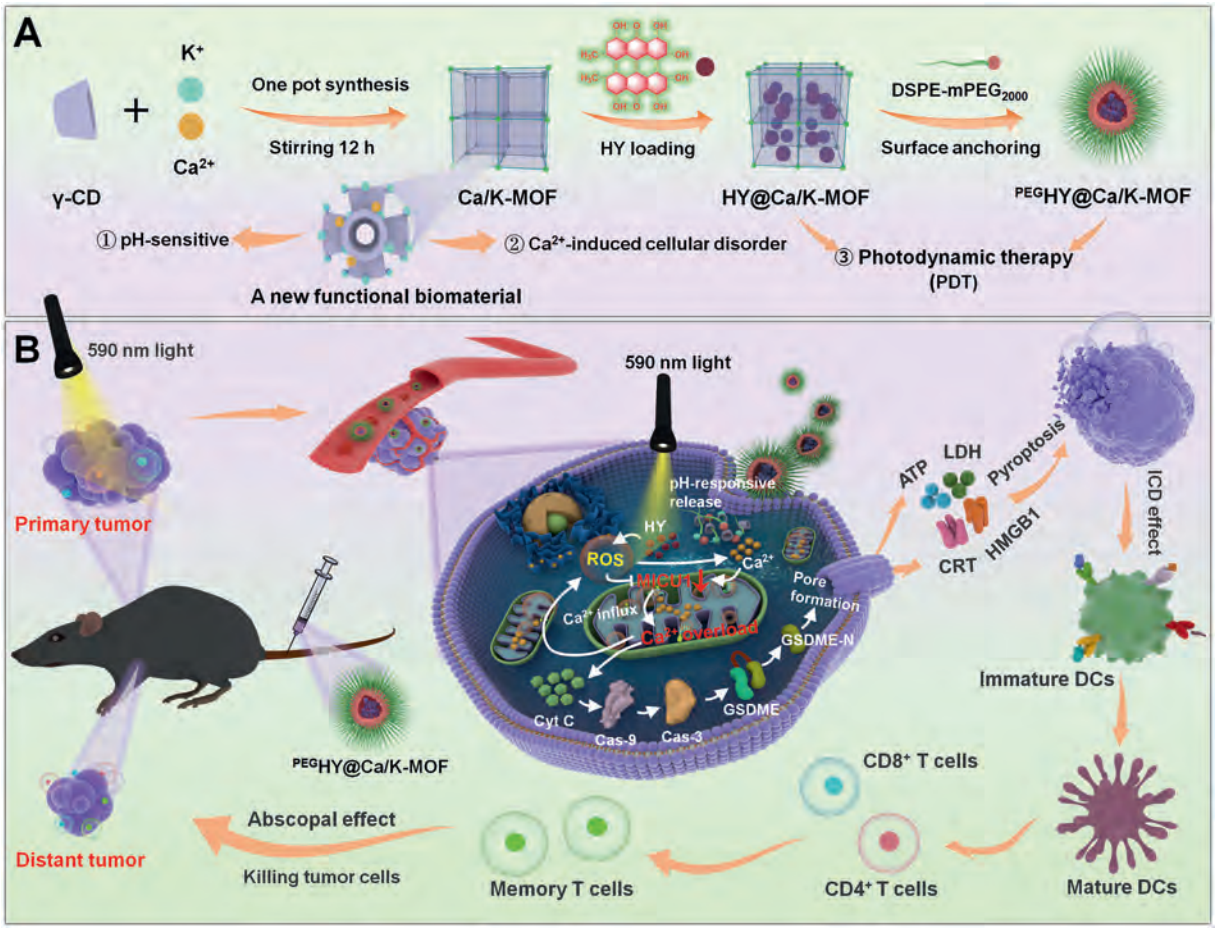

Scheme 1 Schematic illustration of the construction of Ca-doped CD-MOF (Ca/K-MOF) for HY loading (^{PEG}HY@Ca/K-MOF) and its application in comprehensive cancer therapy. (A) Schematic illustration of Ca/K-MOF as a novel carrier material with acid-sensitive, drug-encapsulating properties and potential biological activity. HY was then encapsulated within Ca/K-MOF to form ^{PEG}HY@Ca/K-MOF, demonstrating capabilities for photo-controlled mitochondrial Ca^{2+} influx. (B) ^{PEG}HY@Ca/K-MOF-mediated photo-controlled mitochondrial Ca^{2+} overload-induced pyroptosis to amplify immune responses to tumor cells.

covalency between the metal active site and its surrounding coordination environment. The computational model of 12.5% Ca-doped MOF (denoted as III) closely aligns with our experimental sample of Ca-doped MOF ($Ca_{0.2}/K_{1.4}$-MOF). Guided by the preceding theoretical calculations, we chose $Ca_{0.2}/K_{1.4}$-MOF for subsequent investigation, hereafter referred to as Ca/K-MOF for brevity.

As shown in Fig. 1E and Supporting Information Fig. S1, in comparison with K-MOF, Ca/K-MOF preserved its cubic morphology, which is consistent with the SEM observations (Fig. 1A). Fig. 1F shows the AC-HAADF-STEM images of Ca/K-MOF, revealing the atomic dispersion of Ca and K species within the Ca/K-MOF. In addition, as characterized by ICP-OES verification, the Ca content in Ca/K-MOF was confirmed to be 1.2% (*w*/*w*), while the K content was determined to be 3.43% (*w*/*w*) (Fig. 1G). The EDS element mapping images and the corresponding EDS spectrum clearly show the uniform distribution of C, O, K, and Ca elements throughout the entire hybrid material (Fig. 1H and Supporting Information Fig. S2). Subsequently, we investigated the crystal structures of the MOF prior to and following Ca doping using XRD analysis. As shown in Fig. 1I, the absence of a distinct $CaCl_2$ crystalline phase was compelling evidence that Ca atoms are homogeneously doped into the MOF matrix. The XRD pattern of Ca/K-MOF, exhibiting peaks at $2\theta = 5.32°$, 7.04°, 8.20°, 10.00°, 13.52° and 16.76°, matching well with the simulated pattern of γ-CD-MOF[25], confirming the successful doping. This observation indicates that Ca/K-MOF maintains its original crystal structure post-doping, signifying the successful incorporation of Ca. Meanwhile, XPS was applied to detect the chemical state of surface elements in both K-MOF and Ca/K-MOF. The distinct Ca signal detected by XPS indicated the presence of Ca single-atoms within the Ca/K-MOF structure (Fig. 1J). In the high-resolution XPS spectrum, the Ca 2p core level exhibits a spin-orbital splitting doublet at 346.28 eV ($2p_{3/2}$) and 349.68 eV ($2p_{1/2}$)[26]. The binding energies of the K active site's 2p orbitals decrease from 295.48 and 292.78 to 295.08 and 292.38 eV upon Ca^{2+} introduction, confirming the modification of the electronic environment surrounding both K and Ca[27]. Furthermore, the O 1s peaks in the Ca-doped CD-MOF shift negatively to lower binding energies in contrast to the pristine K-MOF, signifying an increased electron density at the O atoms. The C 1s peaks observed at 284.1, 285.7, and 287.1 eV were well-fitted with C−C, C−O, and O−C−O bonds, respectively.

XAFS spectra were conducted to further clarify the local geometric and electronic structures of Ca/K-MOF (Fig. 1K−M). The Ca K-edge X-ray absorption near-edge structure (XANES) spectra indicate that the pre-edge feature of Ca/K-MOF was quite close to that of CaO, suggesting that the valency of Ca is near +2. The coordination environment of Ca was further examined by

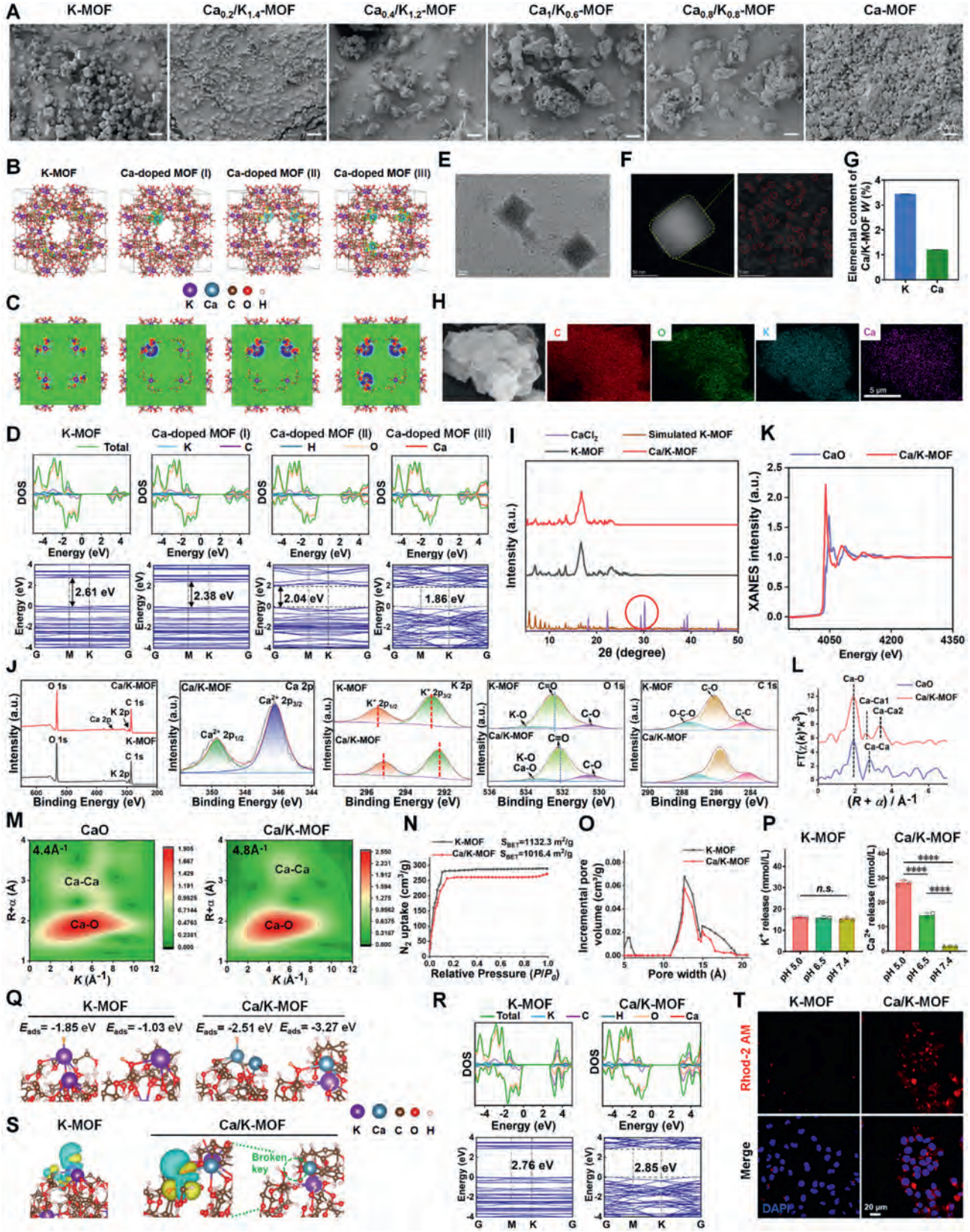

extended X-ray absorption fine structure (EXAFS) analyses. A dominant peak at 1.9 Å in the Ca/K-MOF spectrum aligns with the expected Ca−O coordination distance, confirming the bond formation between Ca and O. Additionally, the small peak at 2.6 Å could be indicative of Ca−Ca interactions[28,29]. Compared with the peak intensity corresponding to Ca−O coordination, the significantly weaker peak of Ca−Ca coordination indicates a smaller proportion of Ca clusters and the atomically dispersed nature of Ca species in Ca/K-MOF. We fitted the Fourier transform XAFS in the R-space of Ca K-edge using the structure model of replacing K atoms in K-MOF with Ca atoms. As shown in Supporting Information Table S2 and Fig. S3, the fitting spectrum is well consistent with Ca as measured, further confirming that Ca single-atom replaced a portion of the K atoms within the Ca/K-MOF structure. The Morlet wavelet transform (MWT) of EXAFS spectra is a powerful analytical method for qualitatively identifying and directly visualizing the local bonding structure of metal atoms, as well as identifying overlapping contributions caused by the multiple-scattering phenomenon. The MWT of the k3-weighted EXAFS spectra for Ca in both CaO and Ca/K-MOF are shown in Fig. 1M. The MWT contour plots show a maximum intensity at approximately 4.4 $Å^{-1}$ in k-space, which is assigned to the scattering paths for Ca−O and Ca−Ca in CaO. Concurrently, the maxima for both Ca−O and Ca−Ca were observed at 4.8 $Å^{-1}$ in the Ca/K-MOF spectrum.

The measured Brunauer-Emmett-Teller (BET) surface areas for K-MOF and Ca/K-MOF were determined to be 1132.3 and 1016.4 m^2/g, respectively. The pore size distribution analysis of both MOFs shows that their pore maxima are centered at 12.6 Å, providing compelling evidence for the successful occupation of K-coordinated ion sites by Ca ions (Fig. 1N and O). Furthermore, the Ca doping ratio of 1:1 was also determined (Supporting Information Fig. S4). The N_2-accessible surface area of $Ca_{0.8}/K_{0.8}$-MOF almost decreased to 0 m^2/g, indicating that the porosity of the MOF is nearly eliminated once the calcium doping ratio surpasses a certain threshold. This finding is consistent with the observations taken from the SEM images shown in Fig. 1A. The water contact angle indicates the hydrophilic property of K-MOF and Ca/K-MOF (Supporting Information Fig. S5). The initial contact angle for Ca/K-MOF was 67.2°, which is higher than that of K-MOF at 55.1°, but it reduced to 51.5° upon stabilization. This suggests that Ca/K-MOF ultimately exhibits improved hydrophilicity. The fluctuating contact angle of Ca/K-MOF during measurement is hypothesized to result from the initial interaction of water molecules with the calcium clusters on the MOF surface, followed by a gradual infiltration into the MOF's internal cavity. The introduction of water-repellent Ca^{2+} can improve the moisture resistance of the MOFs. This Ca^{2+} doping on the surface of MOF shielded it from direct exposure to moisture, thereby effectively preventing hydrolysis[30].

Next, we investigated the release of Ca^{2+} and K^+ ions in a simulated acidic TME. The Ca^{2+} release from Ca/K-MOF exhibited a pH-dependent behavior. After a 12-h incubation in NaH_2PO_4/Na_2HPO_4 buffers at varying pH levels (5.0, 6.5, and 7.4), the Ca^{2+} concentration in the supernatant solution was quantified. As shown in Fig. 1P and Supporting Information Fig. S6, the concentration of released Ca^{2+} from the Ca-doped MOF was notably enhanced by the increased acidity of the media. Meanwhile, the K^+ concentration of Ca/K-MOF mirrored similar trends, whereas the K^+ release from K-MOF remained unaffected across different pH treatments. These findings reveal that Ca doping in Ca/K-MOF introduces a new property: pronounced acid responsiveness.

To further shed light on the underlying mechanism of the pH-responsive behavior of Ca-doped MOF, we conducted DFT calculations. Initially, under the simulated acidic microenvironment of the tumor, the optimal H^+ adsorption sites for both Ca/K-MOF and K-MOF were screened by proposing the possible adsorption models. As shown in Fig. 1Q, the geometrically optimized structures for both K-MOF and Ca/K-MOF, along with the adsorption energy (E_{ads}), were utilized to characterize the interaction between H^+ and the MOFs. From the various candidate adsorption models, we choose the ones exhibiting the higher adsorption energy for each MOF for subsequent computational analysis, corresponding to E_{ads} values of −1.85 eV for K-MOF and −3.27 eV for Ca/K-MOF.

In general, the higher the adsorption energy, the more effectively it facilitates the binding of free electrons and the accumulation of protons. Therefore, when compared to K-MOF, which had an adsorption energy of 1.85 eV, Ca/K-MOF exhibited a larger H^+ adsorption energy of 3.27 eV. This indicated that it was easier to adsorb H^+ due to the optimization of the electronic structure,

Figure 1 Ca/K-MOF emerging as a potential candidate for enhanced acid responsiveness and bioactivity. (A) SEM images of Ca-doped MOFs with various Ca doping ratios. Scale bar = 20 μm. (B, C) Theoretical calculations of optimized geometrical structure (B) and charge density difference plots (C) of K-MOF and Ca-doped MOFs with various doping levels. Ca-doped MOF (I): Ca/K = 4.2%; Ca-doped MOF (II): Ca/K = 8.3%; and Ca-doped MOF (III): Ca/K = 12.5%. (D) Theoretical analysis of the bandgap-narrowing effect induced by increased Ca-doping density. The upper portion represents theoretical calculations of the density of states (DOS), while the lower portion depicts theoretical calculations of band structure. (E) TEM image of Ca/K-MOF at a Ca/K ratio of 1:7. Scale bar = 20 nm. (F) AC-HAADF-STEM images of Ca/K-MOF. (G) ICP-OES analysis showing the calculated elemental content of Ca and K in Ca/K-MOF. (H) Elemental mapping of the as-prepared Ca/K-MOF showing the distribution of C, O, K, and Ca. Scale bar = 5 μm. (I) XRD patterns of Ca/K-MOF and its individual components. (J) X-ray photoelectron spectroscopy (XPS) analysis for chemical bonding information of K-MOF and Ca/K-MOF. (K) Normalized Ca, K-edge XANES spectra of Ca/K-MOF and CaO. (L) FT-EXAFS spectra of the CaO and Ca/K-MOF. (M) Wavelet transform plots of Ca, K-edge in CaO and Ca/K-MOF. (N) BET analysis for N_2 absorption patterns of K-MOF and Ca/K-MOF. (O) Pore size distributions of K-MOF and Ca/K-MOF. (P) The release profiles of K^+ from K-MOF and Ca^{2+} from Ca/K-MOF after 12-h incubation in NaH_2PO_4/Na_2HPO_4 media at different pH levels (5.0, 6.5, and 7.4). $n = 3$, *n.s.* represents no significant difference, $****P < 0.0001$. (Q) The DFT calculation showing the adsorption energy (E_{ads}) of H^+ on different constructed models of MOFs. (R) Theoretical analysis showing the DOS and band energy of K-MOF and Ca/K-MOF after H^+ adsorption. (S) The local charge density distribution in K-MOF and Ca/K-MOF after adsorption of H^+. Yellow and blue regions denote the accrual and expenditure of electrons. The Bader charge analysis reveals that the charge states of H^+ adsorbed in K-MOF pre- and post-adsorption are 0.43 |e| and 0.35 |e|, while for H^+ adsorbed in Ca/K-MOF, the charge states are 0.58 |e| and 0.13 |e|, respectively. (T) CLSM assessment of mitochondrial Ca^{2+} production in B16F10 cells stained with Rhod-2 AM (red) following treatment with K-MOF or Ca/K-MOF. Scale bar = 20 μm.

thus accelerating the accumulation of protons and benefiting the formation of a local acidic environment on the Ca sites. Subsequent analysis of the band structure and DOS reveals that the interaction strength of H^+ and the pristine MOF was comparatively weaker compared to the doped MOF (Fig. 1R). Additionally, the variation in DOS before and after adsorption was minimal, with diminished fluctuations at the Fermi energy level. The Bader charge analysis delineates the charge transfer phenomena between atoms, both prior to and following the bond formation[31]. Fig. 1S shows the distribution of local charge density subsequent to H^+ adsorption, with blue and yellow colors representing a decrease and an increase in electron density, respectively. Upon H^+ adsorption, the Bader charge value associated with the doped MOF's Ca−O bond (0.13 |e|) was lower than that of the original MOF's K−O bond (0.35 |e|). This disparity suggests a reduced bond strength for the Ca−O linkage, implying that the Ca−O bond is more prone to cleavage. Consequently, this provides a theoretical basis for the enhanced release of calcium ions in the acidic milieu surrounding Ca/K-MOF. Based on the theoretical analysis provided, it can be inferred that the doping of Ca endows pH-sensitive property upon the MOF.

On the other hand, the bioactivity of new materials is also frequently a subject of interest. Under normal physiological conditions, the concentration of intracellular Ca^{2+} is in equilibrium, and an excessive concentration can lead to cellular dysfunction. Therefore, to investigate the biological effects of Ca/K-MOF, we traced tumor cells after contact with Ca/K-MOF using the mitochondrial calcium ion probe Rhod-2 AM. The results indicated that, compared to K-MOF, the novel Ca-doped MOF more readily induced an obvious increase in intramitochondrial calcium levels (Fig. 1T), demonstrating that Ca/K-MOF can disrupt the concentration of intracellular Ca^{2+}, potentially regulating the growth of tumor cells. These findings suggest that Ca/K-MOF, while maintaining its drug-loading capability, represents a novel class of safe carrier materials characterized by acid-responsive properties and exhibiting potential biological effects through Ca^{2+} interference.

3.2. *Synthesis and characterization of ^{PEG}HY@Ca/K-MOF*

Given that Ca/K-MOF maintains its drug-loading capabilities, we encapsulated the photosensitizer hypericin within Ca/K-MOF (HY@Ca/K-MOF) *via* a solvent impregnation method. After repeated washing to remove unstable surface adsorbates, robust encapsulation of hypericin within Ca/K-MOF was achieved. Besides, DSPE-mPEG_{2000} was anchored to the surface of HY@Ca/K-MOF (^{PEG}HY@Ca/K-MOF) to improve its dispersibility and stability under physiological conditions[32]. After loading with HY, TEM observation revealed that the HY@Ca/K-MOF had almost inherited the cubic structure and uniform size distribution (Fig. 2A), indicating that such a Ca-doped MOF provides a hydrophobic interface for MOF, which protects the framework from collapsing. The ^{PEG}HY@Ca/K-MOF maintained a spherical structure while ensuring the integrity of the HY@Ca/K-MOF (Fig. 2A). After PEGylated modification, the DLS data showed the average hydrodynamic particle size from 306 ± 24 to 356 ± 33 nm, and the polydispersity index (PDI) value shifted from 0.236 ± 0.014 to 0.175 ± 0.011 (Fig. 2B). The larger size measurements obtained by DLS could be due to the Brownian motion of MOF particles in the liquid medium, which encompasses several layers of solvent molecules surrounding the particles. The zeta potential values of Ca/K-MOF, HY@Ca/K-MOF, and ^{PEG}HY@Ca/K-MOF were −16.13 ± 0.53, −23.22 ± 0.62, and −10.92 ± 0.65 mV, respectively (Supporting Information Fig. S7). This indicates that HY was successfully loaded onto Ca/K-MOF and modified with DSPE-mPEG_{2000}. The loading content of HY in ^{PEG}HY@Ca/K-MOF was 23.4 wt%, which is higher than that in HY@Ca/K-MOF (15.6 wt%) and HY@K-MOF (16.2 wt%) (Fig. 2C). Meanwhile, compared with HY@Ca/K-MOF, the loading contents of Ca elements in ^{PEG}HY@Ca/K-MOF did not exhibit any noticeable alteration (Fig. 2D). Subsequently, to evaluate the biocompatibility of ^{PEG}HY@Ca/K-MOF, a hemolysis assay was conducted. No obvious hemolysis was observed, even at high concentrations of ^{PEG}HY@Ca/K-MOF (Fig. 2E). Additionally, it was discovered that ^{PEG}HY@Ca/K-MOF remained stable without any aggregation after incubation in PBS, cell medium, and serum for 48 h, in contrast to HY@K-MOF and HY@Ca/K-MOF (Fig. 2F), showing the stability of the final formulation in these three environments, which made it extremely suitable for both *in vitro* and *in vivo* antitumor applications.

The FT-IR spectrum reveals that the Ca/K-MOF maintained the characteristic peaks of K-MOF at 3479, 2926, and 1658 cm^{-1} (Fig. 2G). When compared to HY, the spectra of HY@K-MOF and HY@Ca/K-MOF showed diminished absorption bands at 1460 and 1421 cm^{-1}, with some characteristic peaks of HY even disappearing, which confirmed that the HY molecules were encapsulated within the cavities of the MOFs. As shown in Supporting Information Fig. S8, the ^{1}H NMR spectrum of Ca/K-MOF closely matches the previously reported K-MOF[33], and the characteristic peaks of pure HY are consistent with the literature[34]. However, it is noteworthy that the HY signal in the HY-loaded Ca/K-MOF spectrum showed distinct changes, including the disappearance of signals at 14.69 and 14.05 ppm, and the emergence of new signals at 5.36 and 8.45 ppm. This shift likely results from the encapsulation of HY within the Ca/K-MOF framework[35]. The DSC thermograms, shown in Supporting Information Fig. S9, indicated that, aside from the endothermic peak caused by moisture at 110 °C, pure HY exhibited no obvious peaks within the temperature range of 25−350 °C, a characteristic indicative of its amorphous state. The melting exothermic peaks of the prepared K-MOF and Ca/K-MOF appeared at slightly lower temperatures than the corresponding HY-loaded MOF, and the melting exotherms were broader, this may be ascribed to the nude MOF having a huge surface area. The thermal stability of both empty and HY-loaded Ca/K-MOF was investigated using TGA. As shown in Supporting Information Fig. S10, the mass loss of MOFs from 30 to 200 °C is related to the evaporation loss of water and the presence of other impurities in the samples. The thermal degradation of Ca/K-MOF and K-MOF occurred at approximately 200 °C, aligning with the literature-reported results for K-MOF[33]. Notably, the residual amount of HY@Ca/K-MOF (19.83%) was higher than that of HY (15.15%), likely due to the encapsulation of HY within the cavities of Ca/K-MOF[36].

Next, we brought the perspective to the evaluation of the photodynamic performance of ^{PEG}HY@Ca/K-MOF. Firstly, compared with dispersed HY and HY@K-MOF, the fluorescence emission of HY@Ca/K-MOF and ^{PEG}HY@Ca/K-MOF was sharply enhanced (Supporting Information Fig. S11). This suggests that Ca-doped MOF can mitigate the aggregation-caused quenching effects of HY, likely due to the increased steric hindrance provided by its characteristic porous structure[37]. In other words, the spatial confinement effect of Ca/K-MOF restricts molecular aggregation. The photostability of

the various samples was evaluated (Fig. 2H). After 100 min of irradiation (20 mW/cm^2), ^{PEG}HY@Ca/K-MOF and HY@Ca/K-MOF showed photodegradation rates of 12.7 ± 2.7% and 12.3 ± 2.5%, respectively, compared to Free HY (36.2 ± 4.5%) and HY@K-MOF (41.3 ± 3.3%), indicating that Ca ion doping was conducive to improving photostability, a result owed to the cavity structure of Ca/K-MOF, which alleviated the optical quenching effect of HY.

Afterward, to further investigate the PDT capability of ^{PEG}HY@Ca/K-MOF, the generation of $^1O_2$ under 590 ± 10 nm LED irradiation was characterized using the singlet oxygen trapping agent DPBF probe, which could be oxidized by $^1O_2$ to decrease its signature absorption peak at 415 nm[38]. The progressive reduction in the absorption peaks of DPBF over irradiation time confirmed the ongoing production of $^1O_2$ (Fig. 2I). As expected, the absorption intensity of DPBF solution containing ^{PEG}HY@Ca/K-MOF declined more rapidly than that of the other groups, a result of the enhanced generation of $^1O_2$, underscoring the exceptional PDT efficacy of ^{PEG}HY@Ca/K-MOF (Fig. 2J and K). Additionally, the fluorescence lifetime (FLT) and quantum yields (QYs) of the two Ca-doped HY-loaded MOFs were markedly improved compared to HY@K-MOF (Fig. 2L and M). Therefore, the introduction of Ca in HY-loaded MOF offered substantial advantages in fluorescence performance over their undoped counterparts. It is well-established that the conversion of O_2 to $^1O_2$ entails a process involving the transformation of energy and the transfer of electrons. The ground state of O_2 ($^3O_2$) features two unpaired electrons occupying separate antibonding π orbitals (π_x* and π^{y*}), whereas the excited state of O^2 ($^1O_2$) has paired electrons in the antibonding π orbital (π_x*)[39,40]. Referring to the DOS results of K-MOF and Ca/K-MOF (Fig. 1D), upon doping MOF with Ca, interfacial effects of HY@Ca/K-MOF were established through mutual adsorption. Under 590 nm light, the leptonic electrons can trigger more charge transfers, providing O_2 with increased access to electrons and energy. This leads to a significant reduction in the energy threshold for O_2 activation within this structure. Consequently, it facilitates the transition of O_2 from its ground state to the excited state, thereby enhancing the generation of $^1O_2$. In general, the introduction of Ca for the synergistic coordination can break the symmetric structure of the γ-CD-MOF, thus changing the local charge distribution of the active center and causing distortion of the electron density for much improved photodynamic performance.

Lastly, to confirm whether the HY-loaded Ca/K-MOFs retained the acid-responsiveness of Ca/K-MOF, we examined their morphology and drug release profile at various pH levels. Contrasting with the intact morphology of HY@Ca/K-MOF and ^{PEG}HY@Ca/K-MOF in pH 7.4 medium, a segment of the outer wall of these materials' structure disintegrated and collapsed under pH 6.5 conditions (Fig. 2N). In the medium adjusted to pH 5.0, no intact MOF or PEGylated nanosphere structures were observed, as they entirely crumbled. In striking contrast, we also observed that HY@K-MOF, under the same conditions, did not exhibit any notable disintegration or dissolution behavior (Supporting Information Fig. S12). Similarly, Ca^{2+} and K^+ ions in both HY@Ca/K-MOF and ^{PEG}HY@Ca/K-MOF inherited the acid-responsive properties of Ca/K-MOF, while HY@K-MOF behaved in accordance with the characteristics of K-MOF (Fig. 2O and Supporting Information Fig. S13). Consistently, the release behavior of the drug HY kept aligning with the aforementioned findings (Fig. 2P and Q). Regardless of the pH conditions, the release profile of HY from HY@K-MOF remained unchanged; however, in the doped formulations HY@Ca/K-MOF and ^{PEG}HY@Ca/K-MOF, the release of HY exhibited distinct acid sensitivity.

The aforementioned results indicate that HY@Ca/K-MOF and ^{PEG}HY@Ca/K-MOF have retained the acid sensitivity and potential bioactivity of Ca/K-MOF. Furthermore, the introduction of Ca^{2+} has significantly enhanced HY's optical properties and its ability to generate $^1O_2$ in ^{PEG}HY@Ca/K-MOF, which is beneficial for PDT. Furthermore, as a γ-cyclodextrin-modified organic carrier, Ca/K-MOF demonstrates superior biocompatibility and drug-loading capabilities compared to inorganic calcium-based carriers. Collectively, these findings convincingly illustrate that ^{PEG}HY@Ca/K-MOF holds outstanding prospects for controllable drug delivery.

3.3. In vitro cellular activity assessment

To investigate the cellular uptake of HY-loaded MOFs in B16F10 cells, CLSM was utilized to track the cellular uptake behaviors of HY inside the B16F10 cells (Fig. 3A and Supporting Information Fig. S14A). At both 0.5 and 4 h, numerous red signals from HY@Ca/K-MOF and ^{PEG}HY@Ca/K-MOF within the cells were observed in greater quantities compared to Free HY, which is associated with the characteristic ease with which nanoformulations are internalized by cells[41-43]. The corresponding quantitation results from flow cytometry analysis were consistent with CLSM observation (Fig. S14B).

Next, we evaluated the antitumor effect of ^{PEG}HY@Ca/K-MOF *in vitro* by MTT assay. The viability of B16F10 cells treated with Ca/K-MOF was markedly reduced compared to the K-MOF group, likely due to the efficient inflow of Ca^{2+} (Fig. 3B), indicating that Ca/K-MOF gains biological activity by causing intracellular Ca^{2+} disruption. Furthermore, the cell viability did not significantly alter at varying concentrations of HY in the absence of 590 nm irradiation for both Free HY and HY@K-MOF. Under these conditions, Ca^{2+} could reduce the viability of cells treated with HY. This effect was further amplified under light irradiation. Therefore, formulations that include HY, Ca^{2+}, and light (20 mW/cm^2, 5 min), such as HY@Ca/K-MOF and ^{PEG}HY@Ca/K-MOF, can more effectively inhibit cell proliferation (Fig. 3C). It should be noted that cells treated with ^{PEG}HY@Ca/K-MOF under light irradiation (^{PEG}HY@Ca/K-MOF + L) displayed the lowest survival rate, which was owing to the synergistic therapeutic effects of photo-induced ROS and Ca^{2+} overload. Simultaneously, the survival of normal cells (RAW 264.7 cells and FHC cells) after treatment with Ca-doped MOFs showed decreased toxicity (Supporting Information Fig. S15). It is evident that the corresponding IC_{50} values for normal cells were much higher than those for tumor cells, which is due to the fact that calcium-related signaling pathways are differently remodeled for survival in tumor cells compared to normal cells, resulting in heightened sensitivity to intracellular Ca^{2+} in tumor cells[44]. Consistent with the aforementioned findings, HY-containing formulations significantly induced apoptosis under the influence of light irradiation and this therapeutic effect was sensitized by the presence of Ca^{2+}. Consequently, ^{PEG}HY@Ca/K-MOF + L exhibited a stronger apoptotic efficiency (Fig. 3D and Supporting Information Fig. S16), highlighting the enhancement effect of Ca^{2+} overload in the context of ROS generation induced by light.

3.4. Light-controlled bidirectional amplification effect of ROS and Ca^{2+} overload through MICU1 downregulation

The mechanism of action of light-controlled mitochondrial Ca^{2+} overload warrants further exploration. Initially, we determined

mitochondrial Ca^{2+} levels in B16F10 cells following various treatments by using a mitochondria isolation kit and a calcium assay kit. Clearly, Free HY did not induce any changes in Ca^{2+} concentration during the culture process (Fig. 3E). However, the intramitochondrial calcium level in the group treated with Free HY under light irradiation was 6.7-fold higher than that in the control group (Fig. 3F), indicating that light exposure might lead to the accumulation of Ca^{2+} within the mitochondria. It is hypothesized that this could be attributed to light-induced ROS surge causing mitochondrial damage, the scrambling and disturbance of

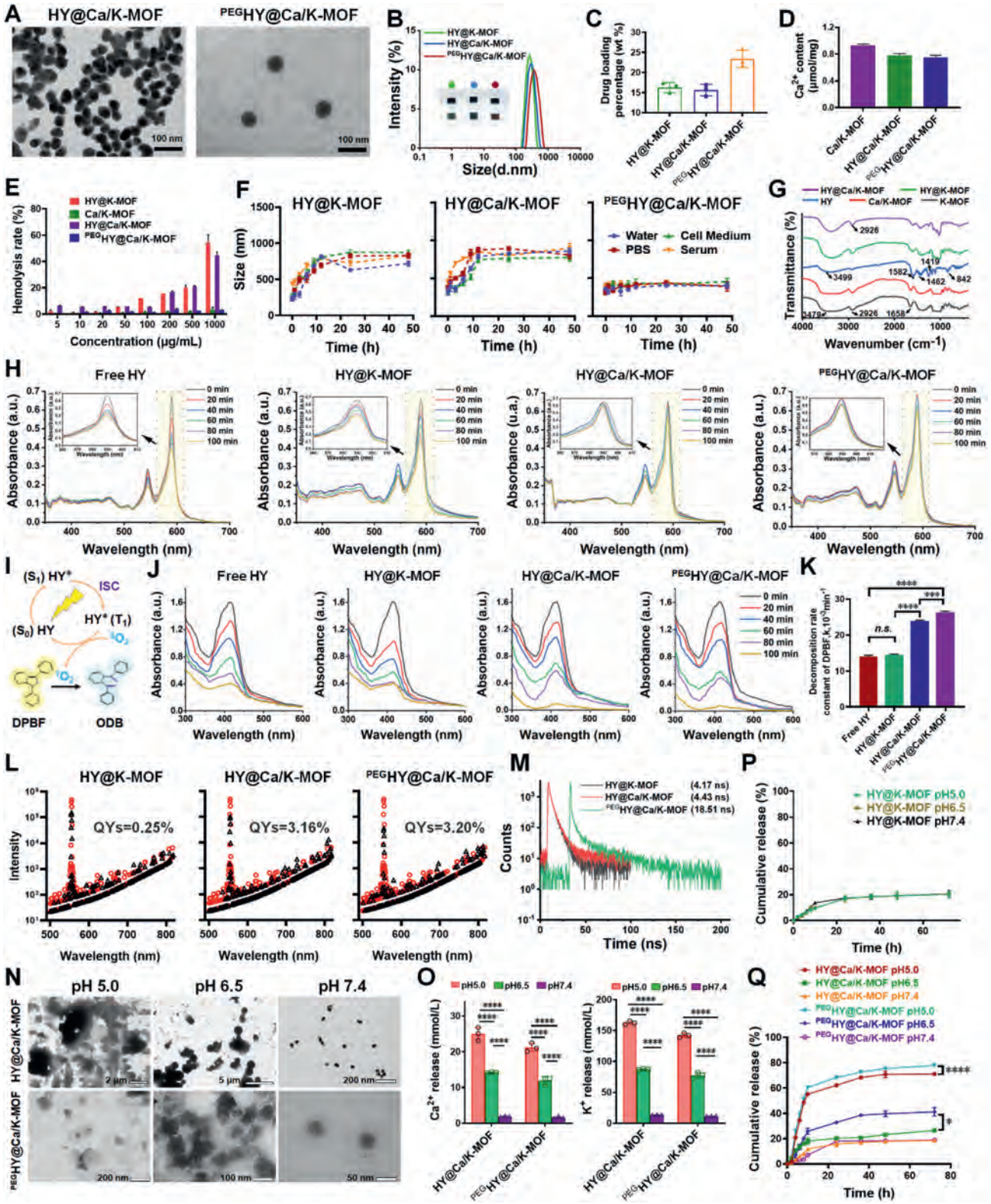

the mitochondrial membrane channels responsible for Ca^{2+} accumulation, and the subsequent influx of Ca^{2+} from the cytoplasm into the mitochondria. Additionally, free HY inhibited the efflux of Ca^{2+} from the cytoplasm to the extracellular fluid following 590 nm light exposure, resulting in an elevation of the intracytoplasmic Ca^{2+} concentration. The Ca^{2+}-doped groups exhibited a notably higher mitochondrial calcium content compared to their non-doped counterparts, and this effect could be further significantly intensified by light exposure.

Both CLSM and flow cytometry analysis indicated that after cellular uptake, HY@Ca/K-MOF and ^{PEG}HY@Ca/K-MOF significantly increased the intracellular Ca^{2+} concentration (Fig. 3G and H and Supporting Information Fig. S17), which was further elevated under light exposure (Fig. 3H). The Ca/K-MOF group showed stronger green fluorescence intensity than the undoped MOF group, which verified the effective influx of calcium ions. In all groups treated with HY-containing formulations, the fluorescence intensity was stronger with light irradiation than without (Fig. 3G and H), indicating that ROS generated by photodynamic effects can promote an increase in Ca^{2+} concentration. It is speculated that this may be because HY induced by light can trigger a strong membrane puncture, which subsequently leads to a high extracellular Ca^{2+} inward flow. Therefore, we refer to the phenomenon of ^{PEG}HY@Ca/K-MOF with light irradiation inducing Ca^{2+} overload in the mitochondria of cancer cells as photo-controlled Ca^{2+} dysregulation.

Previous studies have indicated that the buildup of cytosolic Ca^{2+} can stimulate the activity of multiple dehydrogenases involved in the tricarboxylic acid cycle, which is responsible for ROS generation, and Ca^{2+}-induced electron leakage from the respiratory chain further promotes ATP synthesis and elevates ROS levels[45-48]. We then assessed the generation of ROS in B16F10 cells using the 2′,7′-dichlorofluorescein diacetate (DCFH-DA) probe. The fluorescence intensity in cells treated with Ca/K-MOF was significantly enhanced compared to the negligible fluorescence observed in the K-MOF group (Fig. 3I and J and Supporting Information Fig. S18), confirming that the increase in intracellular Ca^{2+} concentration induced by the Ca-doped MOF can effectively enhance the accumulation of intracellular ROS. In parallel, the HY@Ca/K-MOF and ^{PEG}HY@Ca/K-MOF groups presented more intense green fluorescence than the Free HY or HY@K-MOF groups, effectively leading to tremendous ROS generation under 590 nm laser irradiation. However, this effect caused by HY@Ca/K-MOF + L and ^{PEG}HY@Ca/K-MOF + L could be reversed by a calcium chelator of BAPTA-AM or an oxidative stress inhibitor of ascorbic acid (VC) (Fig. 3K and Supporting Information Fig. S19). These results confirm that ^{PEG}HY@ Ca/K-MOF could boost ROS production, collaboratively due to the doping of calcium ions and the enhanced PDT efficiency of HY. Complementarily, the exogenous calcium ions derived from the Ca-doped MOFs and the endogenous calcium ions triggered by ROS, which are a byproduct of the photodynamic activity of the HY, reciprocally contributed to the mitochondrial Ca^{2+} overload that may lead to cellular dysfunction.

Given that overloaded Ca^{2+} influx and excessive ROS accumulation can trigger mitochondrial damage and dysfunction[49], we tested mitochondrial membrane potential (MMP) changes using the membrane-permeant Rh123 probe, which enters mitochondria based on their membrane potential, causing fluorescence to fade. If the membrane is damaged, the potential drops, releasing Rh123 and producing bright yellow-green fluorescence. As depicted in Fig. 3L and M, all the cells treated with different Ca-doped MOFs exhibited lower MMP levels than the corresponding monometallic ligand MOFs. Among them, benefiting from the supercharged photodynamic activity of HY, the cells treated with ^{PEG}HY@Ca/K-MOF + L had the sharpest green fluorescence intensity, indicating the lowest MMP and the most severe mitochondrial damage. The above result is quantitatively supported by the flow cytometry results (Supporting Information Fig. S20). Furthermore, all three HY-loaded MOF + L groups exhibited varied degrees of mitochondrial microstructural damage compared to the control group (Fig. 3N). Specific manifestations include the mitochondria swelling, inner range breakage, disappearing, and becoming air-vacuolated. Notably, the ^{PEG}HY@Ca/K-MOF, with light exposure, produced the most severe mitochondrial swelling, which was accompanied by a significant decrease in electron density of the inter-cristae matrix, a disappearance of matrix granules, a presence of more flocculent amorphous protein disintegration products within the inner cavity of mitochondria, and a disorganization of the cristae structure. Furthermore, we observed mitochondrial condensation and coalescence, the emergence of round, vacuolated mitochondria, and even the presence of mitophagosomes. These results indicate that ^{PEG}HY@Ca/K-MOF, upon exposure to 590 nm light, possesses a remarkable capacity to impair mitochondria. Given that mitochondrial Ca^{2+} overload also triggers mitochondrial damage[50], it is speculated that oxidative stress from HY PDT might initially induce mitochondrial damage. This initial injury could then dramatically exacerbate mitochondrial Ca^{2+} overload, further promoting oxidative stress and mitochondrial damage. This vicious cycle would likely amplify the therapeutic effects observed in B16F10 cells.

In an overall assessment of the molecular mechanism, we employed immunoblot analysis to assess the expression levels of

Figure 2 Synthesis and characterization of ^{PEG}HY@Ca/K-MOF. (A) TEM images of HY@Ca/K-MOF and ^{PEG}HY@Ca/K-MOF. Scale bar = 100 nm. (B) The particle size distribution of HY@K-MOF, HY@Ca/K-MOF, and ^{PEG}HY@Ca/K-MOF. Inset: digital photographs of HY@K-MOF (green), HY@Ca/K-MOF (blue), and ^{PEG}HY@Ca/K-MOF (red) solutions. (C) Comparative HY loading capacities of MOFs at equivalent dosages. (D) Ca^{2+} content in different Ca-doped MOFs. (E) Hemolysis assessment at varying MOF concentrations. (F) Stability of HY-loaded MOFs determined by DLS in water, PBS, cell medium, and serum over a 48-h period. (G) FT-IR spectra of different MOF formulations. (H) Photostability evaluation of different irradiation durations. (I) Schematic illustration of the mechanism of DPBF for $^1O_2$ detection. (J) Absorbance spectra of DPBF and HY-loaded MOFs post-irradiation at various time intervals (0, 20, 40, 60, 80, and 100 min) with an LED source at 590 ± 10 nm. (K) Rate constants for the decomposition of DPBF in HY-loaded MOFs. (L) Quantum yields of HY-loaded MOFs (λ_{ex} = 555 nm). (M) Typical fluorescence decay profiles of HY-loaded MOFs. The excitation wavelength was 475 nm, and the emission was collected in the wavelength range of 475−600 nm using a bandpass filter. (N) TEM images showing the morphology of HY@Ca/K-MOF and ^{PEG}HY@ Ca/K-MOF in different pH buffers. (O) The release profiles of Ca^{2+} and K^+ from HY@Ca/K-MOF and ^{PEG}HY@ Ca/K-MOF after 12-h incubation in media at different pH levels (5.0, 6.5, and 7.4). (P, Q) The release profiles of HY for HY@K-MOF (P) and Ca-doped MOFs (Q) at different pH levels of 5.0, 6.5, and 7.4. $n = 3$, *n.s.* represents no significant difference, $^*P < 0.05$, $^{***}P < 0.001$, $^{****}P < 0.0001$.

proteins associated with Ca^{2+} homeostasis in B16F10 cells (Fig. 3O and Supporting Information Fig. S21). CALPAIN1, a Ca^{2+}-activated protein that amplifies and initiates death signaling in the cytosol, showed increased expression (Fig. 3O) in Ca-doped groups and HY-containing groups with light irradiation, reflecting the enrichment of Ca^{2+} levels within the tumor cells[51].

The plasma membrane Ca^{2+} ATP2B4 (PMCA4) is tasked with pumping Ca^{2+} out of the cell into the extracellular space.

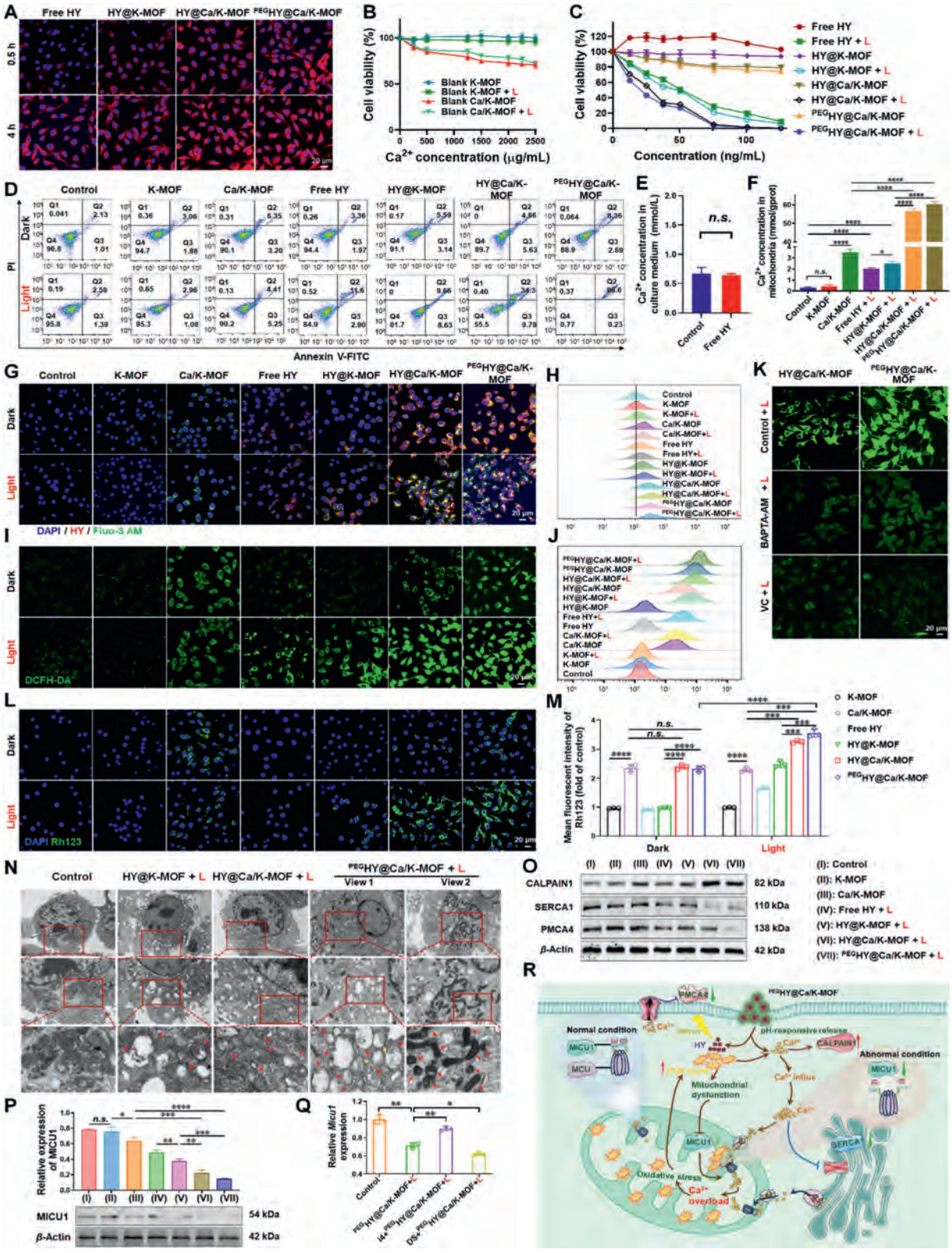

However, elevated ROS or "oxidative stress", can hinder this exocytosis by suppressing PMCA4 activity, thus trapping calcium within the cytoplasm[52,53]. Our tests convincingly demonstrated that the ^{PEG}HY@Ca/K-MOF + L group, which generated the most ROS, also experienced the most significant inhibition of PMCA4.

The sarcoplasmic reticulum Ca^{2+} ATP2A1 (SERCA1), an ATP-dependent pump on the endoplasmic reticulum (ER), actively transports Ca^{2+} from the cytoplasm into the ER. The ER is known to interact structurally and functionally with mitochondria. It has been reported that inhibiting SERCA1 can promote calcium leakage from the ER, thereby facilitating its entry into the mitochondria[54-56]. Compared to the control, the Free HY + L group showed a significant reduction in SERCA1 expression, indicating that HY-generated ROS can effectively inhibit Ca^{2+} transport to ER sites. This was further supported by the ^{PEG}HY@Ca/K-MOF + L group presenting the lightest immunoblot signal among the Ca-doped groups, indicating a substantial inhibition of SERCA1.

Mitochondrial calcium overload is primarily associated with the mitochondrial calcium uniporter (MCU), which is situated in the inner mitochondrial membrane and selectively transports Ca^{2+}. The MCU's activity is modulated by the mitochondrial calcium uniporter regulator 1 (MCUR1), which enhances its function, and the mitochondrial calcium uptake 1 (MICU1), which inhibits it. It is known that changes in MICU1 expression can cause mitochondrial calcium overload; MICU1, acting as an MCU inhibitor, directly regulates MCU activity, and its downregulation leads to sustained Ca^{2+} influx into mitochondria, thereby increasing mitochondrial ROS production[49,57-63]. We then investigated whether our Ca-doped MOFs could decrease MICU1 expression, thereby causing mitochondrial calcium overload. Western blot analysis indicated that Ca-doped MOFs suppressed MICU1 expression to different extents, with ^{PEG}HY@Ca/K-MOF + L exhibiting the most potent inhibitory effect (Fig. 3P). This finding was further validated by RT-qPCR, which detected significant changes in *Micu1* expression in the ^{PEG}HY@Ca/K-MOF + L-treated group following treatment with the *Micu1* activator MCU-i4 (i4) or the calcium uptake regulatory protein inhibitor DS16570511 (DS) (Fig. 3Q, Supporting Information Table S3 and Fig. S22)[64,65]. Immunofluorescence assays confirmed the expression levels of PMCA4 and MICU1, consistent with the results from the Western blot experiments (Supporting Information Figs. S23 and S24). This suggests that effective intervention of ^{PEG}HY@Ca/K-MOF with light can allow significant downregulation of MICU1 expression.

To elucidate the relationship between ROS and MICU1, we employed either an ROS inhibitor (VC) or an ROS generator (VK) for intervention. The observed disparity in MICU1 expression between the VK group and the control groups, as shown in Supporting Information Fig. S25, further provides additional evidence that ROS generation can suppress MICU1 protein expression. This finding is corroborated by the comparative performance of the ^{PEG}HY@Ca/K-MOF + L group, which showed a significantly lower *Micu1* expression compared to the VC and VC + ^{PEG}HY@Ca/K-MOF + L groups. Subsequently, as shown in Supporting Information Fig. S26, we also assessed the effect of altered MICU1 expression on intramitochondrial Ca^{2+}. When tumor cells were pretreated with the MICU1 activator i4 or the calcium uptake regulatory protein inhibitor DS, the mitochondrial Ca^{2+} content in ^{PEG}HY@Ca/K-MOF + L-treated cells was significantly decreased or increased, respectively, proving that down-regulation of MICU1 triggers calcium influx into mitochondria. Meanwhile, the inverse relationship between MICU1 expression and ROS generation was also confirmed by flow cytometry (Supporting Information Fig. S27). Overall, photodynamic activity following HY light irradiation leads to mitochondrial dysfunction. The potent oxidative effect of ROS generated from PDT suppresses MICU1 expression on the mitochondrial inner membrane. Consequently, the diminished MICU1 expression allows for increased Ca^{2+} influx into the mitochondria, resulting in a light-controlled mitochondrial calcium overload. This overload, in turn, synergistically amplifies ROS-mediated oxidative stress, establishing a vicious cycle of oxidative stress and calcium overload that exacerbates mitochondrial damage (Fig. 3R).

3.5. Light-controlled mitochondrial Ca^{2+} overload-triggered pyroptosis

Motivated by the potentiated state of intracellular mitochondrial calcium overload, the pyroptosis properties were further investigated. As shown in Fig. 4A, B16F10 cells treated with Free HY or

Figure 3 ^{PEG}HY@Ca/K-MOF induces calcium ion disruption, mitochondrial calcium overload, and a photodynamic effect in B16F10 cells. (A) Confocal images of cellular uptake following treatment with Free HY, HY@K-MOF, HY@Ca/K-MOF, and ^{PEG}HY@Ca/K-MOF at 0.5 and 4 h. Scale bar = 20 μm. (B) Cell viability of B16F10 cells after treatment with K-MOF or Ca/K-MOF with or without 590 nm light irradiation for 5 min (20 mW/cm^2). "L" denotes irradiation with 590 nm light. (C) Cytotoxicity of Free HY, HY@K-MOF, HY@Ca/K-MOF, or ^{PEG}HY@Ca/K-MOF with different concentrations toward B16F10 cells with or without 590 nm irradiation (20 mW/cm^2, 5 min). (D) Cell apoptosis analysis of B16F10 cells under different treatments. (E) No influence of Free HY on the fluctuation of Ca^{2+} concentration in the culture medium. (F) The influences of various treatments on mitochondrial Ca^{2+} concentrations in B16F10 cells. (G, H) CLSM (G) and flow cytometry (H) analysis of B16F10 cells in various groups after using the Fluo-3 AM probe to monitor the Ca^{2+} influx. (I, J) Representative CLSM images (I) and flow cytometry (J) showing ROS generation stained by DCFH-DA after different treatments. (K) Representative CLSM images of ROS levels after treatment with HY@Ca/K-MOF or ^{PEG}HY@Ca/K-MOF in the presence of calcium chelator or ROS inhibitor (BAPTA-AM at 10 μmol/L or VC at 0.5 mmol/L). (L, M) CLSM (L) and corresponding quantitative (M) analysis of mitochondrial membrane potential alterations following incubation with different treatments. Scale bar = 20 μm. (N) Representative Bio-TEM images of mitochondrial integrity after different treatments. The red arrows represent damaged mitochondria, and the yellow arrows represent mitophagosomes. (O) The expression levels of calcium-regulated proteins, including CALPAIN1, SERCA1, and PMCA4, in B16F10 cells after different treatments. (P) Western blotting and corresponding quantitation analysis of calcium uptake−associated mitochondrial protein (MICU1) expression in B16F10 cells with β-actin used as the loading control. (I): Control, (II): K-MOF, (III): Ca/K-MOF, (IV): Free HY + L, (V) HY@K-MOF + L, (VI): HY@Ca/K-MOF + L, (VII): ^{PEG}HY@Ca/K-MOF + L. (Q) RT-qPCR analysis revealing the expression of *Micu1* gene after being treated with ^{PEG}HY@Ca/K-MOF under 590 nm light in the presence of DS (calcium uptake regulatory protein inhibitor) or i4 (*Micu1* activator). (R) Schematic illustration of light-controlled mitochondrial calcium overload by reducing MICU1 expression. $n \geq 3$, *n.s.* represents no significant difference, $^{*}P < 0.05$, $^{**}P < 0.01$, $^{***}P < 0.001$, $^{****}P < 0.0001$.

HY@K-MOF + L showed clear apoptotic characteristics. In contrast, the subsequent groups deviated from apoptotic features: cells treated with Ca/K-MOF generated a small number of bubbles, HY@Ca/K-MOF + L group showed an increased bubble count, and ^{PEG}HY@Ca/K-MOF under 590 nm laser irradiation led to obvious bubble formation and cellular swelling. This observation likely unveiled the successful and noticeable induction of pyroptosis by mitochondrial Ca^{2+} overload induced by ^{PEG}HY@Ca/K-MOF + L treatment. Furthermore, the extracellular release of lactate dehydrogenase (LDH) and adenosine triphosphate (ATP) levels provides additional evidence supporting the occurrence of pyroptosis (Fig. 4B and C). Generally, the N-terminal domain of GSDME binds to membrane phospholipids, forming transmembrane pores that allow the release of ATP and LDH. We quantified the levels of these molecules in the culture supernatants and found that ^{PEG}HY@Ca/K-MOF + L was the most effective at inducing their release in B16F10 cells. Fig. 4D showed that pre-incubation with BAPTA-AM significantly affected LDH levels in the Ca^{2+}-doped groups, indicating that Ca^{2+} can promote pyroptosis in cells.

Additionally, Western blot assays were conducted to evaluate the expression levels of pyroptosis-related proteins in B16F10 cells (Fig. 4E and Supporting Information Fig. S28). The expression levels of Cytochrome C, Cleaved caspase-3, Cleaved caspase-9, and GSDME-N were significantly up-regulated in the HY@Ca/K-MOF + L and ^{PEG}HY@Ca/K-MOF + L groups relative to the other groups. These results corroborate that the Ca-doped MOF loaded with HY under 590 nm light triggers mitochondrial calcium overload in tumor cells, leading to a subsequent surge in ROS that promotes the opening of calcium-induced permeability transition pores. This sequence of events results in mitochondrial dysfunction, followed by the release of Cytochrome C, which in turn activates Caspases-3 and -9, reversing the cell death pathway from apoptosis into pyroptosis, with Cleaved caspase-3 then cleaving GSDME into its N-terminal fragment, GSDME-N[49,66]. The activation of this pathway is characterized by a down-regulation of full-length GSDME and a concomitant increase in GSDME-N. Notably, as shown in Fig. 4F, the pre-incubation of BAPTA-AM caused a sharp decrease in GSDME-N expression following treatment with

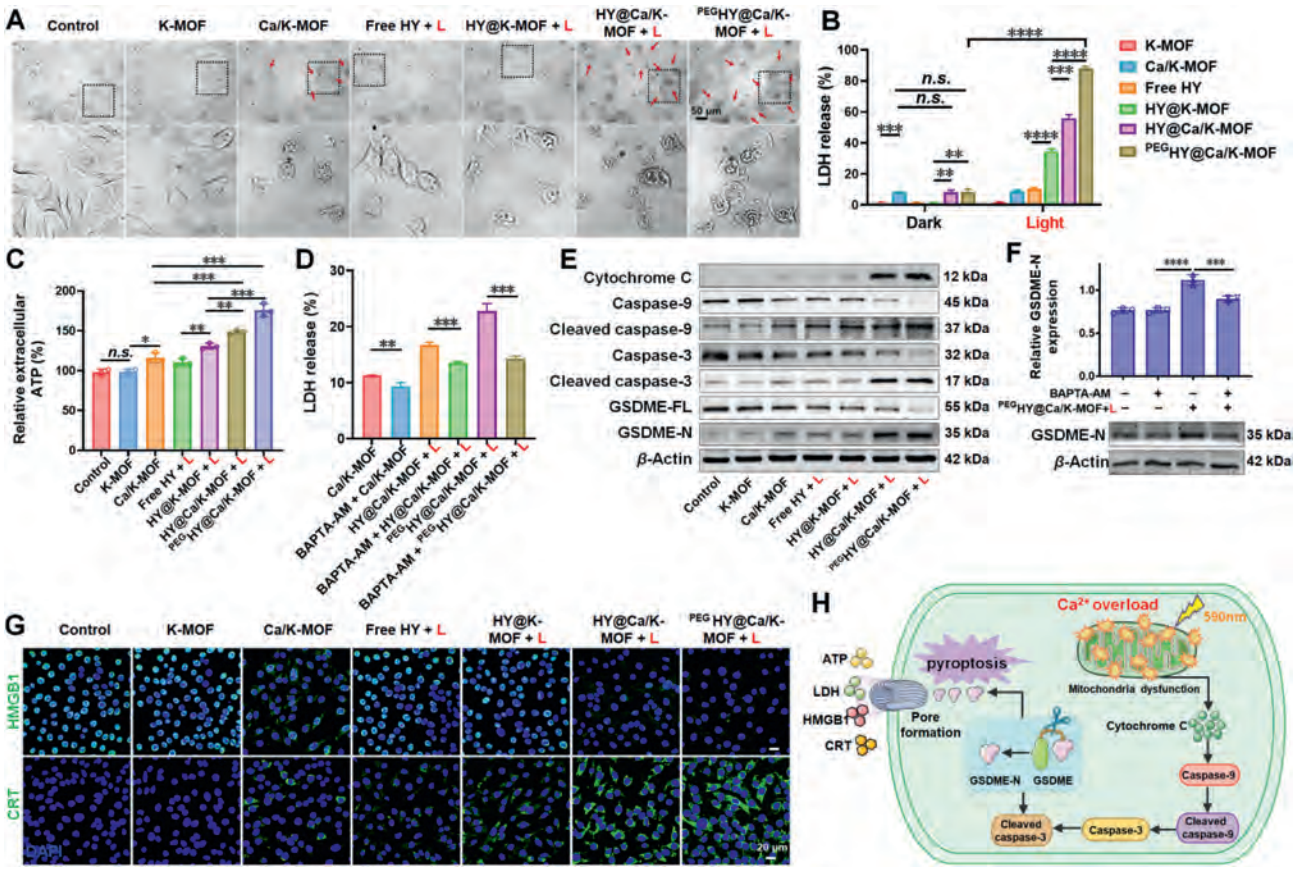

Figure 4 Mitochondrial calcium overload triggers cancer cell pyroptosis. (A) Representative morphological photographs showing B16F10 cell pyroptosis after being treated with various formulations. Scale bar = 50 μm. (B) LDH release from B16F10 cells after different treatments. (C) ATP release from B16F10 cells after different treatments. (D) Inhibition of MOF nanocomposites-induced pyroptosis by calcium ion chelator BAPTA-AM as measured by LDH release in B16F10 cells. (E) Western blotting analysis of pyroptosis-associated protein expression (Cytochrome C, Caspase-9, Cleaved caspase-9, Caspase-3, Cleaved caspase-3, GSDME-FL, and GSDME-N) in B16F10 cells after corresponding treatments. (F) The WB analysis of GSDME-N expression showing chelation of calcium ions inhibits ^{PEG}HY@Ca/K-MOF + L-induced pyroptosis within B16F10 cells. (G) Representative fluorescence images showing HMGB1 migration and CRT exposure in B16F10 cells after different treatments. Scale bar = 20 μm. (H) Schematic illustration of light-controlled calcium overload-induced pyroptosis by ^{PEG}HY@Ca/K-MOF + L. $n \geq 3$, *n.s.* represents no significant difference, $^{*}P < 0.05$, $^{**}P < 0.01$, $^{***}P < 0.001$, $^{****}P < 0.0001$.

^{PEG}HY@Ca/K-MOF under 590 nm light irradiation. This further provides evidence supporting the idea that the onset of pyroptosis is inextricably linked to intracellular mitochondrial calcium overload.

Pyroptosis is commonly known for its distinct immunogenic cell death (ICD) characteristics, including the substantial release of damage-associated molecular patterns (DAMPs)[67]. To validate the immune-activating potential of ^{PEG}HY@Ca/K-MOF, we assessed representative biomarkers of the ICD-associated DAMPs with immunofluorescence including high mobility group protein B1 (HMGB1) and calreticulin (CRT) (Fig. 4G). With Ca^{2+} doping, the HMGB1 signal on the CLSM images gradually changed from bright green in the nucleus to weak green fluorescence localized in the cytoplasm, indicating that HMGB1 was

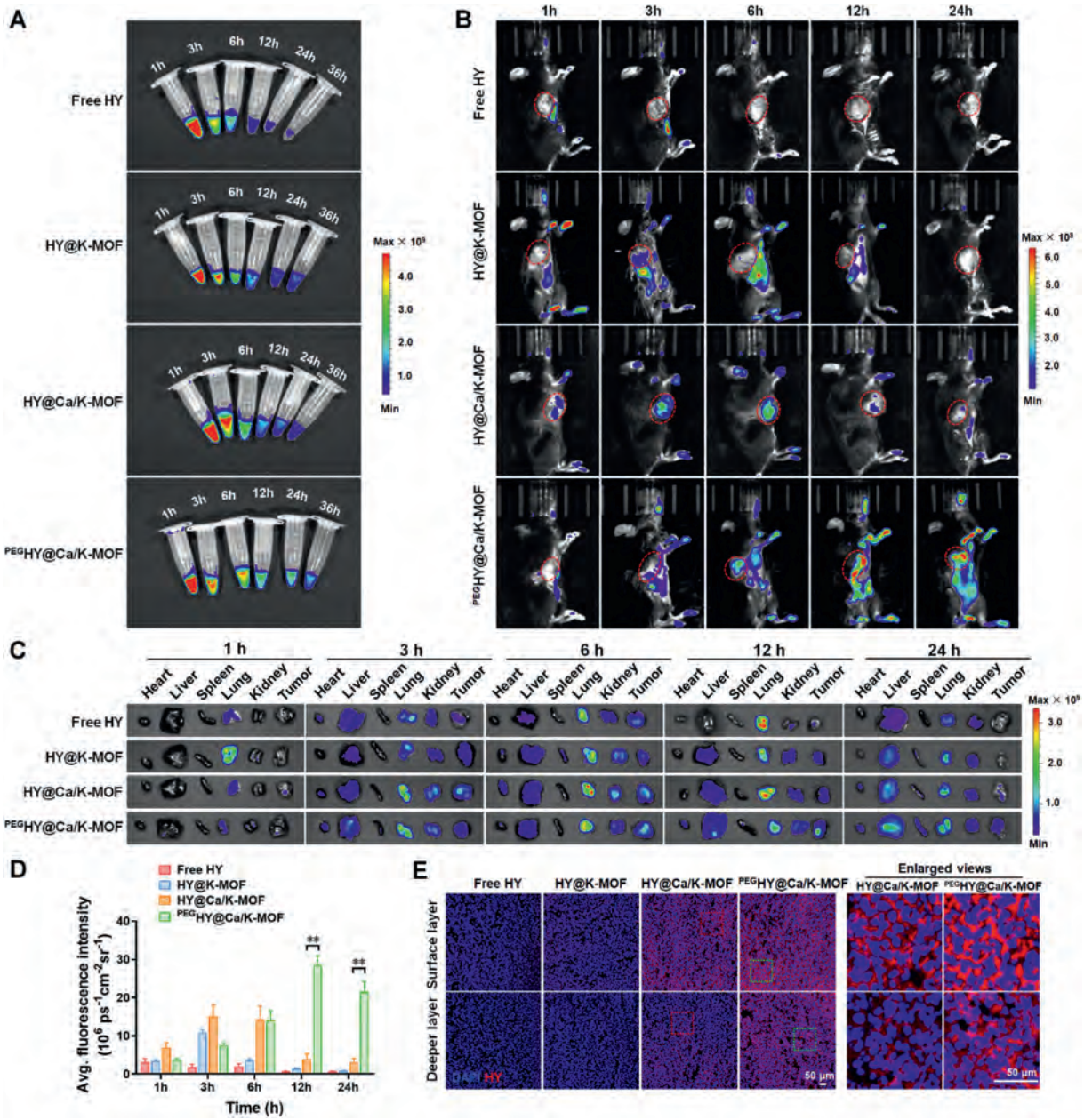

Figure 5 ^{PEG}HY@Ca/K-MOF enhances intratumoral drug accumulation. (A) The temporal circulation profiles of Free HY, HY@K-MOF, HY@Ca/K-MOF, and ^{PEG}HY@Ca/K-MOF in the bloodstream. Blood samples were collected from C57BL/6 mice bearing the B16F10 tumor at various time points following tail vein injections of different formulations and subsequently imaged using a fluorescence imaging system (IVIS, PerkinElmer). (B) Time-lapse biodistribution fluorescence images of whole animals bearing B16F10 xenograft tumors after being treated with Free HY, HY@K-MOF, HY@Ca/K-MOF, and ^{PEG}HY@Ca/K-MOF at 1, 3, 6, 12, 24 h, respectively. (C) Fluorescence signals in excised organs including heart, liver, spleen, lung, kidney, B16F10 tumor after being treated with Free HY, HY@K-MOF, HY@Ca/K-MOF, and ^{PEG}HY@Ca/K-MOF at desired time points. $\lambda_{ex} = 570$ nm, $\lambda_{em} = 620$ nm. (D) Semiquantitative analysis of tumor fluorescence intensity following different HY treatments at multiple time points *in vivo*. (E) Representative confocal images of tumor tissue sections from mice injected with Free HY or HY-loaded MOFs at 12 h post-injection. Blue: DAPI for staining the cell nucleus; red: Free HY or HY-loaded MOFs. Scale bar = 50 μm. $n \geq 3$, $^{**}P < 0.01$.

effectively released into the extracellular matrix. The green fluorescence of CRT was observed on the extracellular membrane after treatments with various Ca^{2+}-doped MOFs. In contrast, the undoped groups including K-MOF, Free HY + L, and HY@K-MOF + L showed slightly weaker changes. As expected, the ^{PEG}HY@Ca/K-MOF group exhibited the highest levels of HMGB1 and CRT release from cells after light exposure. These results highlight the potential of ^{PEG}HY@Ca/K-MOF as a highly

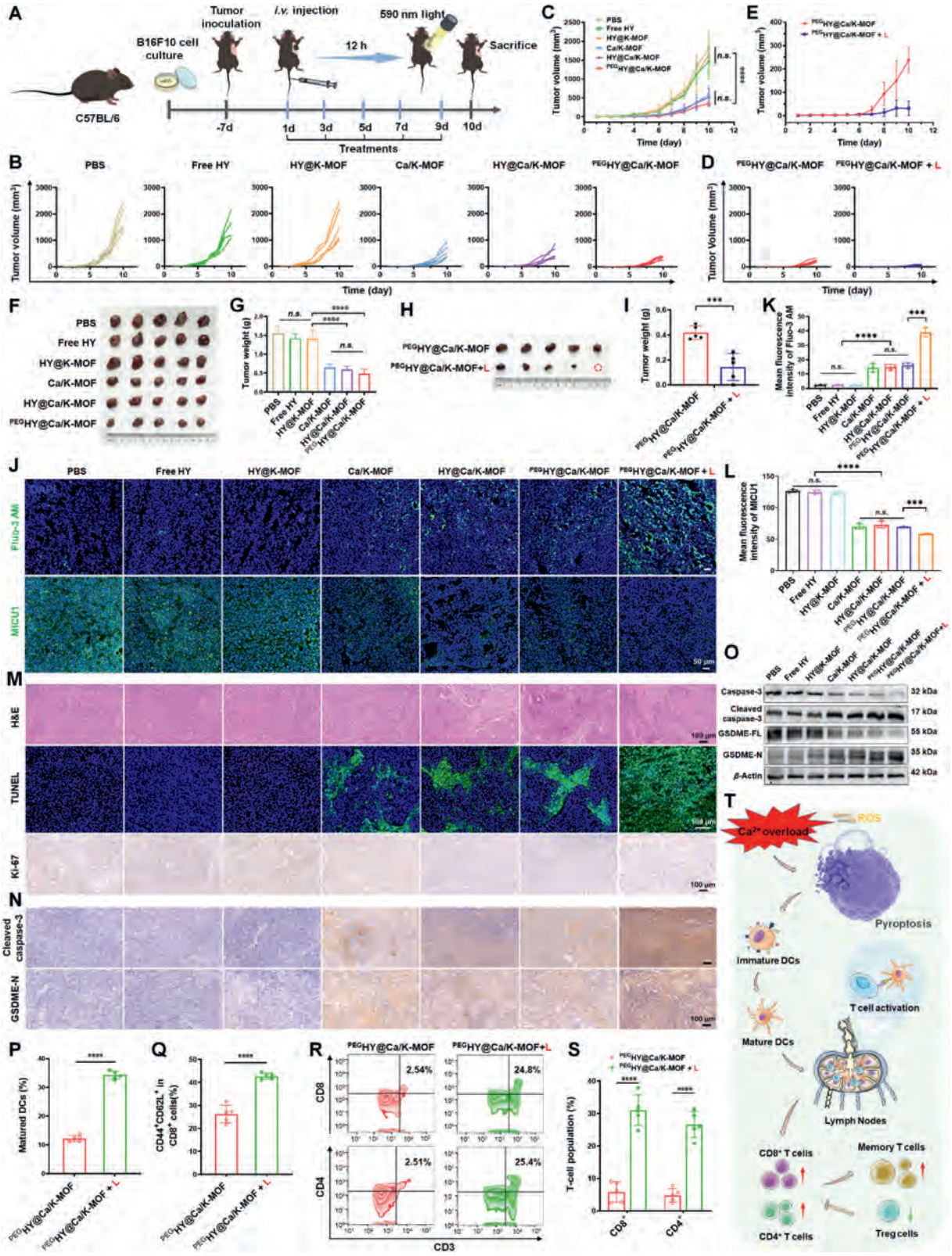

effective generator for inducing the light-controlled mitochondrial Ca^{2+} overload-pyroptosis immunotherapy (Fig. 4H).

3.6. *In vivo fluorescence imaging*

Four groups of C57BL/6 mice, each bearing the B16F10 tumor model, were intravenously (i.v.) injected with Free HY, HY@K-MOF, HY@Ca/K-MOF, and ^{PEG}HY@Ca/K-MOF, respectively. We explored their *in vivo* biodistribution and the corresponding fluorescence of venous blood at different time points using an *in vivo* imaging system (IVIS) (Fig. 5A−D and Supporting Information Fig. S29). As shown in Fig. 5A and Fig. S29, the fluorescence emission in the blood was consistently stronger for the ^{PEG}HY@Ca/K-MOF group compared to the other three groups from 1 to 36 h post-injection, indicating a significant long-term tumor retention effect of ^{PEG}HY@Ca/K-MOF. This enhanced tumor retention is attributed to the DSPE-mPEG_{2000} encapsulated MOF system, which leverages the enhanced permeability and retention (EPR) effect and evades reticuloendothelial system (RES) uptake[68].

One hour post-injection, there was no presence of fluorescence at the tumor site in the Free HY group, whereas fluorescence was observed in all MOF groups (Fig. 5B). The fluorescence intensities at the tumor sites in both Ca-doped MOF groups were much stronger than that of the HY@K-MOF group, with the PEGylated MOF showing particularly enhanced intensity. This enhanced fluorescence can be attributed to the passive targeting ability facilitated by the Ca^{2+} doping. The tumor location exhibited the most intense fluorescence 12 h after the infusion of ^{PEG}HY@Ca/K-MOF. Even at 24 h post-injection, the fluorescence intensity at the tumor site in the ^{PEG}HY@Ca/K-MOF group was still stronger than that of the other groups, suggesting that ^{PEG}HY@Ca/K-MOF could effectively accumulate at the tumor site (Fig. 5C and D). Moreover, to detect the distribution of MOFs in tumor tissues, tumors from mice treated with different formulations were sectioned. Notably, the HY fluorescence signals of the HY@Ca/K-MOF-injected tumors were more intense than those of the HY@K-MOF group (Fig. 5E and Supporting Information Fig. S30). The red fluorescence signals at the deep tumor site in mice injected with HY@Ca/K-MOF were approximately 1.36-fold higher than those in mice injected with HY@K-MOF. The enhanced tumor penetration capacity of the two HY-loaded Ca-doped MOFs was attributed to the acid-sensitivity conferred by Ca^{2+} doping, which improves the targeting of tumor cells. Free drugs released at the tumor site are more likely to infiltrate deeper regions. These results confirmed that ^{PEG}HY@Ca/K-MOF possesses superior passive targeting ability and prolonged tumor retention, thereby potentially enhancing its therapeutic efficacy.

3.7. *In vivo activation of pyroptosis and antitumor immunotherapy*

To evaluate the *in vivo* tumor-suppressing efficacy of ^{PEG}HY@Ca/K-MOF, a melanoma mouse model was established using B16F10 tumor cells. The detailed treatment regimen is shown in Fig. 6A. In the absence of lighting conditions, the tumor growth trajectories for the HY@Ca/K-MOF and ^{PEG}HY@Ca/K-MOF groups closely resembled that of the Ca/K-MOF group (Fig. 6B and C). Tumor growth in all Ca-doped MOF groups exhibited a significantly slower progression compared to the other three groups. Although ^{PEG}HY@Ca/K-MOF alone showed limited antitumor activity, the combination of ^{PEG}HY@Ca/K-MOF with light irradiation yielded the most pronounced inhibition of tumor growth. These results showed the synergistic effect of ^{PEG}HY@Ca/K-MOF + L on inhibiting tumor growth (Fig. 6B−I). Additionally, throughout the treatment duration, body weights and organ indices remained stable across all experimental groups, with no significant intergroup differences (Supporting Information Fig. S31). Further blood biochemical and routine analyses revealed that all parameters were within normal ranges, and no obvious inflammation or organ damage was observed in the H&E staining images (Supporting Information Fig. S32). These findings further validate the exceptional biosafety and biocompatibility of ^{PEG}HY@Ca/K-MOF + L.

Consistent with the *in vitro* studies, the upstream pathways of intratumoral Ca^{2+}-induced pyroptosis were similarly investigated. To assess the Ca^{2+} production ability of ^{PEG}HY@Ca/K-MOF + L *in vivo*, the Ca^{2+} level within tumor tissues was measured using a calcium-sensitive fluorescence probe, Fluo-3 AM. As shown in Fig. 6J and K, the Ca-doped MOFs showed only a modest rise in green fluorescence, which proved that Ca-doped MOFs could

Figure 6 Therapeutic efficacy in a unilateral B16F10 tumor-bearing C57BL/6 mouse model. (A) Schematic diagram of the administration regimen for ^{PEG}HY@Ca/K-MOF intravenous injection and photodynamic therapy in B16F10 tumor-bearing mice. On Day 8 post-B16F10 tumor inoculation, different formulations were administered *via* tail vein injection, followed by continuous photoirradiation treatment at 590 nm, carried out for 5 consecutive sessions with a 12-h interval post-injection. (B) Individual tumor growth kinetics of each mouse treated with PBS, Free HY, HY@K-MOF, Ca/K-MOF, HY@Ca/K-MOF, or ^{PEG}HY@Ca/K-MOF. (C) Average tumor growth curves for mice post-treatment with the same regimens as (B). (D) Individual tumor growth kinetics of each mouse treated with ^{PEG}HY@Ca/K-MOF and ^{PEG}HY@Ca/K-MOF + L. (E) Average tumor growth curves for mice post-treatment with the same regimens as (D). (F, G) Representative xenograft tumor images (F) and weight (G) of the tumor after being treated with PBS, Free HY, HY@K-MOF, Ca/K-MOF, HY@Ca/K-MOF, or ^{PEG}HY@Ca/K-MOF. (H, I) Representative xenograft tumor images (H) and weight (I) of the tumor after being treated with ^{PEG}HY@Ca/K-MOF or ^{PEG}HY@Ca/K-MOF + L. (J) Representative confocal images of Ca^{2+} influx (upper) and MICU1 expression (lower) in tumor tissues after the indicated treatment. Scale bar = 50 μm. (K, L) Semiquantitative analysis of tumor fluorescence intensity from (J) for Ca^{2+} influx and MICU1 expression in tumor tissues. (M) Representative H&E, TUNEL, and Ki-67 staining of tumor tissues after different treatments. Scale bar = 100 μm. (N) Representative pyroptosis-associated staining (Cleaved caspase-3 and GSDME-N) of tumor tissues after different treatments. Scale bar = 100 μm. (O) Western blotting analysis of related protein expression (Caspase-3, Cleaved caspase-3, GSDME-FL, and GSDME-N) in tumor tissues after different treatments. (P) Quantitative evaluation of TDLNs-derived DC maturation after being treated with ^{PEG}HY@Ca/K-MOF or ^{PEG}HY@Ca/K-MOF + L. (Q) Relative quantification of $CD44^+CD62L^+$ T_{CM} cells gating on $CD8^+$ cells in the spleens after the indicated treatment. (R, S) Relative populations of $CD3^+CD4^+$ T cells and $CD3^+CD8^+$ T cells in tumors from mice after the indicated treatment. (T) Schematic illustration of ^{PEG}HY@Ca/K-MOF-mediated pyroptosis induced by photo-controlled mitochondrial Ca^{2+} overload to promote DC maturation. Significance was analyzed by two-way ANOVA with Tukey *post hoc* test for (C), one-way ANOVA with a Tukey *post hoc* test for (G, K, L) and a two-tailed Student's *t*-test for (I, P, Q, S). $n = 5$ independent mice per group, *n.s.* represents no significant difference, $^{***}P < 0.001$, $^{****}P < 0.0001$.

increase the intracellular Ca^{2+} levels in tumor tissues. Upon exposure to 590 nm light, the ^{PEG}HY@Ca/K-MOF + L group clearly displayed a significantly higher level of intracellular green fluorescence of Ca^{2+} compared to the HY@Ca/K-MOF group. Moreover, prior to light exposure, the Ca-doped groups exhibited a reduced expression of MICU1 compared to the other groups. Subsequently, upon the introduction of light, the ^{PEG}HY@Ca/K-MOF + L group displayed the sharpest decrease in cytoplasmic MICU1 expression levels (Fig. 6J, L and Supporting Information Fig. S33).

H&E staining of tumor tissues also showed that the ^{PEG}HY@Ca/K-MOF + L treatment group exhibited severe cytoarchitectural changes and karyopyknosis, more so than the other groups. Mice treated with ^{PEG}HY@Ca/K-MOF + L exhibited the strongest TUNEL fluorescence intensity and the fewest Ki-67-positive cells, suggesting its pronounced pro-apoptotic/pyroptosis ability (Fig. 6M and Supporting Information Fig. S34). Immunoblotting and immunohistochemical analysis of biomarkers expression, including Cleaved caspase-3, Caspase-3, GSDME, and GSDME-N, confirmed the activation mechanism of pyroptosis *in vivo*. The Cleaved caspase-3 and GSDME-N were significantly up-regulated in the ^{PEG}HY@Ca/K-MOF group upon 590 nm light irradiation, compared to the non-irradiated group. This indicates a potent induction of pyroptosis within the tumor tissues, effectively activating the pyroptotic pathway (Fig. 6N, O and Supporting Information Figs. S35 and S36). Taken together, the evidence suggests that ROS signaling causes mitochondrial damage, diminishes MICU1 expression, intensifies calcium overload, triggers Caspase-3 activation, and ultimately leads to pyroptosis through GSDME cleavage.

Therefore, it is worth investigating whether ^{PEG}HY@Ca/K-MOF elicits an immune response in tumors. Dendritic cells (DCs), which are crucial antigen-presenting cells (APCs) in tumor-specific immune responses, were detected in tumor-draining lymph nodes (TDLNs) for signs of maturation[69-71]. As shown in Fig. 6P and Supporting Information Fig. S37, among all non-illuminated groups, the Ca-doped groups without light interference exhibited stronger mature DC activation compared to the other non-irradiated groups. The proportion of mature DCs in the ^{PEG}HY@Ca/K-MOF + L-treated group was 2.8 times higher than in the ^{PEG}HY@Ca/K-MOF group alone. These results suggested that ^{PEG}HY@Ca/K-MOF combined with phototherapy effectively activates immune cells. Moreover, compared to another group, those treated with ^{PEG}HY@Ca/K-MOF + L displayed a drastic increase in the proportion of $CD44^+CD62L^+$ central memory T cells (T_{CM}) in the spleen (Fig. 6Q and Supporting Information Fig. S38). This suggests ^{PEG}HY@Ca/K-MOF + L-triggered pyroptosis may confer immune memory effects, potentially leading to sustained remission and prevention of tumor recurrence.

We also found that the proportion of both $CD8^+$ and $CD4^+$ T cells in the tumors of mice treated with ^{PEG}HY@Ca/K-MOF + L was significantly elevated, being 5.4- and 5.5-fold higher, respectively, compared to the ^{PEG}HY@Ca/K-MOF group (Fig. 6R and S). Immunofluorescence labeling images further corroborated these findings, showing a substantial infiltration of $CD8^+$ T cells into the tumor tissues following treatment with ^{PEG}HY@Ca/K-MOF + L (Supporting Information Fig. S39). In addition, we compared the expression levels of immune-related cytokines—key biomarkers for immune cell function activation, including TNF-α, IFN-γ, and IL-1β—released from tumor tissues following different treatments using immunofluorescence staining (Fig. S39). The levels of TNF-α, IFN-γ, and IL-1β were significantly higher in the tumor tissues of the ^{PEG}HY@Ca/K-MOF + L group than in those of the other groups, further confirming the occurrence of an inflammatory response and the effective activation of the immune system by the treatment. Collectively, the combined therapeutic strategy of ^{PEG}HY@Ca/K-MOF + L, which leverages photo-controlled calcium overload therapy and immunotherapy, also termed photo-controlled mitochondrial Ca^{2+} overload-pyroptosis immunotherapy, not only eradicates tumor cells but also promotes DC maturation through the release of DAMPs, which in turn activate cytotoxic T cells and produce a striking anti-tumor effect (Fig. 6T).

The Ca/K-MOF-based nano-delivery platform demonstrated promise in effectiveness and biocompatibility as a new therapeutic option. However, further steps are needed for clinical translation, such as developing ligand-functionalized MOFs to enhance targeting and reduce off-target effects. Optimizing the Ca-doped MOF structure to control calcium release kinetics and minimize systemic side effects is also recommended.

3.8. Abscopal effect in the bilateral tumor model

Subsequently, motivated by our initial findings, we constructed a bilateral B16F10 melanoma tumor model to verify whether our ^{PEG}HY@Ca/K-MOF, upon phototreatment, could induce systemic immune responses and suppress the growth of distant tumors. As shown in Fig. 7A, the primary tumor was inoculated on the right side of the armpit of each mouse, while the secondary or distant tumor was implanted on the left side 4 days post-primary inoculation. R837, a commercially available agonist of toll-like receptor 7, is recognized for its ability to stimulate the immune system's recognition of cancer cells, thereby improving the efficacy of immunotherapy[72]. It was employed as a positive control to induce the abscopal effect. Firstly, no significant differences in body weight and organ index were observed across the four groups (Supporting Information Fig. S40). As shown in Fig. 7B−E, consistent with our earlier results from the unilateral tumor model, the ^{PEG}HY@Ca/K-MOF + L group exhibited the most pronounced inhibition of primary tumor growth. Furthermore, our observations indicated that ^{PEG}HY@Ca/K-MOF outperformed the administration of R837, a well-established immunostimulatory agonist. Notably, the combination of ^{PEG}HY@Ca/K-MOF with light irradiation showed the most potent anti-tumor effect on both primary tumors and distant tumors. The tumor size in this group was significantly reduced compared to all other groups, suggesting that the treatment effectively elicited a systemic anti-tumor immune response. The regression observed in the distant tumors confirms the successful induction of anti-tumor immunity (Fig. 7F−H).

The photodynamic immune-therapy effect induced by calcium overload was further substantiated through H&E staining of both primary and distant tumors after different therapies (Fig. 7I). We assessed a range of indicators associated with ICD using immunofluorescence staining to reveal the effective activation of anti-tumor immunity by ^{PEG}HY@Ca/K-MOF + L induced cancer cell ICD. Initially, the CRT exposure and extracellular release of HMGB1 in the tumor tissues were determined (Fig. 7J−M). As opposed to the sparse green fluorescent signals observed in the PBS group, treatments with R837 and ^{PEG}HY@Ca/K-MOF triggered a small release of HMGB1 and CRT. However, the combination of ^{PEG}HY@Ca/K-MOF with light irradiation at 590 nm led to the most remarkable increase in HMGB1 and CRT

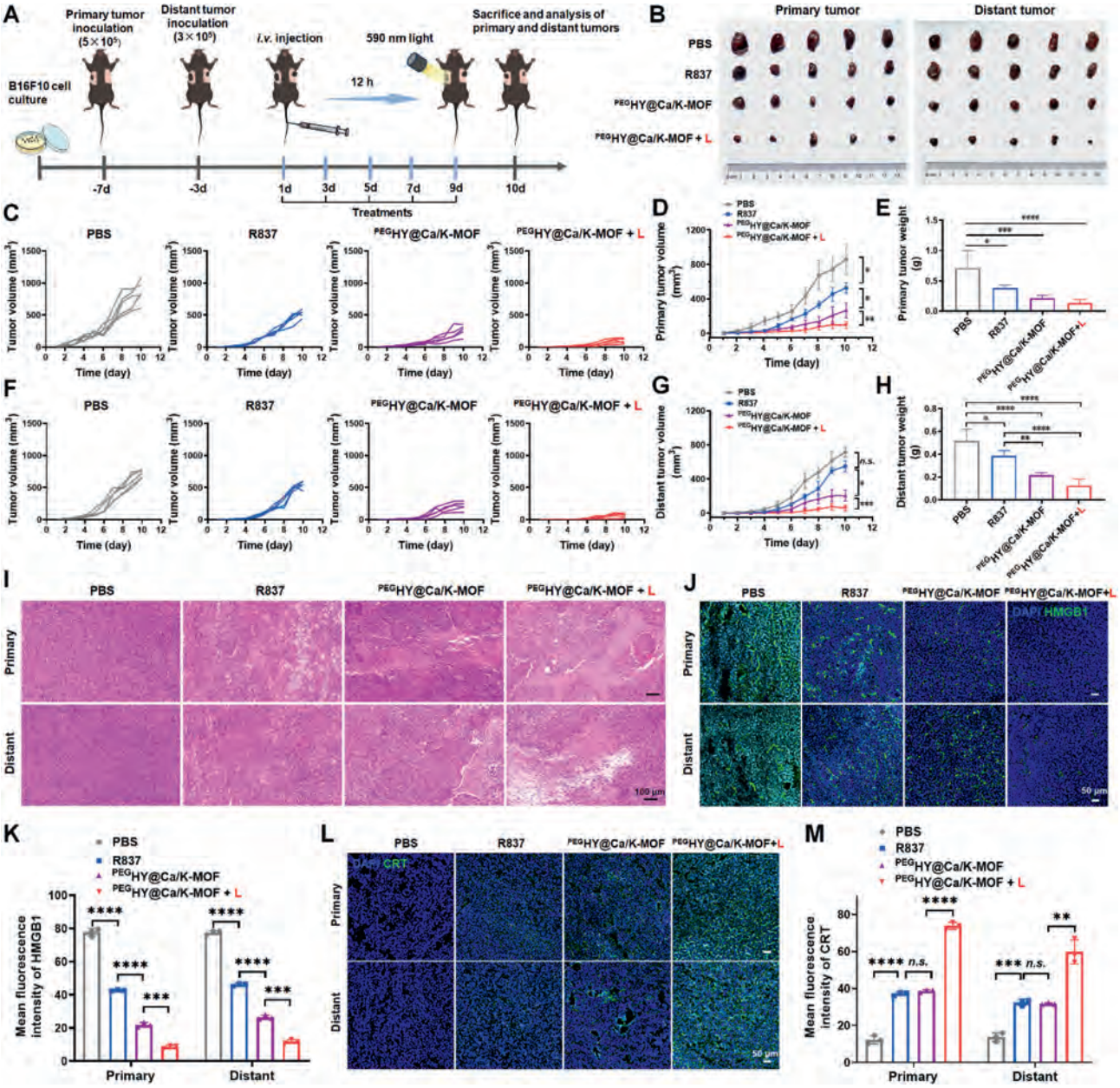

Figure 7 Abscopal effect of ^{PEG}HY@Ca/K-MOF-based Ca^{2+} overload-mediated tumor treatment in a bilateral B16F10 melanoma-bearing mouse model. (A) Schematic illustration of the experimental design for *in vivo* evaluations against primary and distant tumors. (B) Representative photographs of primary tumors and distant tumors in the mice after being treated with PBS, R837, ^{PEG}HY@Ca/K-MOF, or ^{PEG}HY@Ca/K-MOF + L. (C−E) Individual tumor growth kinetics (C), average tumor growth curves (D), and weight (E) of primary tumors in the mice after different treatments. (F−H) Individual tumor growth kinetics (F), average tumor growth curves (G), and weight (H) of distant tumors in the mice after different treatments. (I) H&E analysis of the bilateral tumor after different treatments. Scale bar = 100 μm. (J, K) Representative immunofluorescence images (J) and quantitative analysis (K) of HMGB1 expression in bilateral tumor tissues after different treatments using anti-HMGB1 antibody (green). Scale bar = 50 μm. (L, M) Representative immunofluorescence images (L) and quantitative analysis (M) of CRT expression in bilateral tumor tissues after different treatments using anti-CRT antibody (green). Scale bar = 50 μm. Significance was analyzed by two-way ANOVA with Tukey *post hoc* test for (D, G) and one-way ANOVA with a Tukey *post hoc* test for (E, H, K, M). $n = 5$ independent mice per group, *n.s.* represents no significant difference, $^{*}P < 0.05$, $^{**}P < 0.01$, $^{***}P < 0.001$, $^{****}P < 0.0001$.

exposure. Moreover, our findings indicate that the exposure of ^{PEG}HY@Ca/K-MOF + L resulted in the highest secretion levels of key inflammatory regulators (TNF-α, IFN-γ, and IL-1β) both in the primary and distant tumors compared to all other treatment groups (Supporting Information Fig. S41). These results demonstrated the potent capability of photo-treated ^{PEG}HY@Ca/K-MOF to concurrently induce a robust systemic immune response through proinflammatory pyroptosis.

To gain a deeper understanding of the immune response after different treatments, we assessed DC activation in TDLNs using flow cytometry. The percentages of activated DC (gated at $CD11c^{+}$) in the TDLNs of mice were as follows:

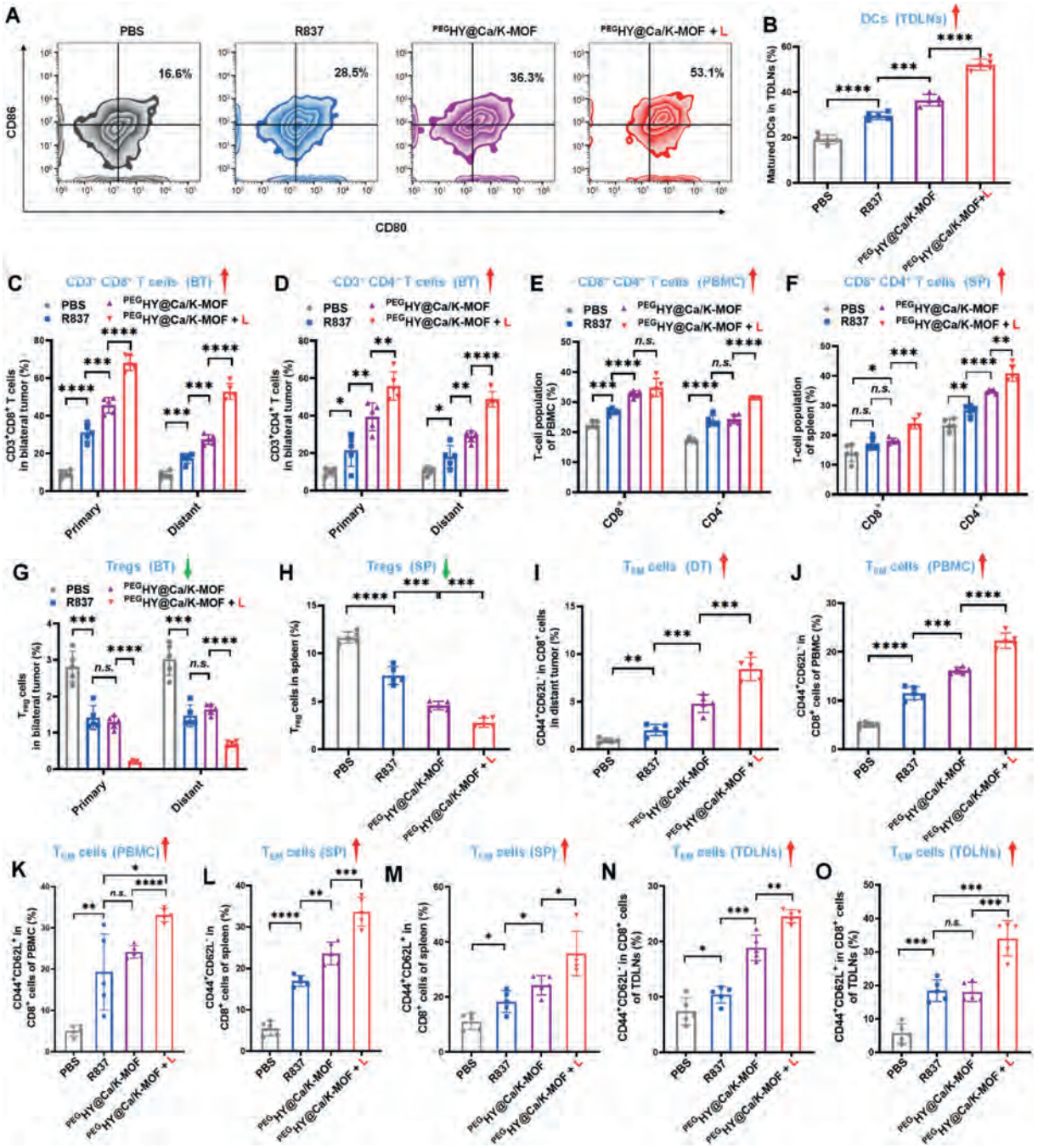

Figure 8 Light-controlled mitochondrial Ca^{2+} overload therapy-enhanced systemic immune responses to ^{PEG}HY@Ca/K-MOF in a bilateral B16F10 melanoma mouse model. (A) Representative flow cytometry plots showing DC maturation in the draining lymph nodes close to the primary tumors after being treated with PBS, R837, ^{PEG}HY@Ca/K-MOF, and ^{PEG}HY@Ca/K-MOF + L. (B) Flow cytometric analysis showing percentages of matured DCs adjacent to the primary tumor-draining lymph nodes (TDLNs) after different treatments. (C, D) Quantitative analysis of $CD3^+CD8^+$ (C) and $CD3^+CD4^+$ (D) T cells in bilateral (primary and distant) tumors (BT) after different treatments. (E, F) Relative proportions of $CD4^+$ and $CD8^+$ T cells in PBMC (E) and spleen (SP) (F) after different treatments. (G, H) Quantitative levels of Treg cells in BT (G) and SP (H) after different treatments. (I) Quantitative analysis of effector memory T cells ($CD44^+CD62L^-$ T_{EM}) in distant tumors (DT) in mice after different treatments. (J, K) Relative quantification of $CD44^+CD62L^-$ T_{EM} (J) and $CD44^+CD62L^+$ T_{CM} (K) cells gating on $CD8^+$ cells in PBMC after different treatments. (L, M) Quantitative analysis of $CD44^+CD62L^-$ T_{EM} (L) and $CD44^+CD62L^+$ T_{CM} (M) cells in the SP after different treatments. (N, O) Relative proportions of $CD44^+CD62L^-$ T_{EM} (N) and $CD44^+CD62L^+$ T_{CM} (O) cells in TDLNs adjacent to the distant tumors after different treatments. $n = 5$ independent mice per group, $^*P < 0.05$, $^{**}P < 0.01$, $^{***}P < 0.001$, $^{****}P < 0.0001$.

19.22 ± 1.73% for the PBS group, 29.66 ± 1.46% for the R837 group, and 36.48 ± 2.24% for the ^{PEG}HY@Ca/K-MOF group. These values were approximately 2.7-, 1.7-, and 1.4-fold lower, respectively, compared to the group treated with light-controlled ^{PEG}HY@Ca/K-MOF, which exhibited the highest level of DC activation at 52.10 ± 2.20% (Fig. 8A and B and Supporting Information Fig. S42). Coinciding with such a tendency, the ^{PEG}HY@Ca/K MOF + L treatment led to a remarkable increase in the numbers of cytotoxic T-cells (labeled $CD3^+CD8^+$) and helper T-cells (labeled $CD3^+CD4^+$) in both primary and distant tumors (Fig. 8C and D and Supporting Information Fig. S43). Similarly, a significant elevation in T cell infiltration was clearly observed in peripheral blood mononuclear cells (PBMCs) and spleen following photo-irradiation treatments with ^{PEG}HY@Ca/K-MOF (Fig. 8E and F and Supporting Information Figs. S44 and S45). In contrast to the PBS group, the levels of suppressive regulatory T cells (T_{reg}), characterized as $CD4^+CD25^+Foxp3^+$, were significantly suppressed in both primary and distant tumors among the R837, ^{PEG}HY@Ca/K-MOF, and ^{PEG}HY@Ca/K-MOF + L treatment groups. Notably, the ^{PEG}HY@Ca/K-MOF + L group exhibited a substantial decrease in T_{reg} frequencies, with 0.22% in primary tumors and 0.59% in distant tumors. These values represented a 6.8-, 5.5-, and 2.6-, 2.8- fold reduction in primary and distant tumors, respectively, compared to the R837 and ^{PEG}HY@Ca/K-MOF groups (Fig. 8G and Supporting Information Fig. S46).

Further analysis of T_{reg} cells in the spleens yielded similar results, indicating that ^{PEG}HY@Ca/K-MOF could effectively relieve the immunosuppressive TME (Fig. 8H and Supporting Information Fig. S47). Additionally, CLSM images and semiquantitative results also revealed that the bilateral tumors in the ^{PEG}HY@Ca/K-MOF + L group exhibited remarkably higher infiltration of $CD8^+$ T cells and a reduced proportion of $Foxp3^+$ regulatory T cells compared to the other three groups (Supporting Information Figs. S48 and S49). Moreover, to assess the long-term effects on immune memory, we detected the levels of $CD8^+$ effector memory T cells ($CD8^+CD44^+CD62L^-$) in distant tumors after different treatments. As illustrated in Fig. 8I and Supporting Information Fig. S50, the proportion of effector memory T cells in distant tumors was significantly enhanced after treatment with ^{PEG}HY@Ca/K-MOF + L. Simultaneously, we analyzed the populations of central memory cells (T_{CM}, $CD44^+CD62L^+$) and effector memory cells (T_{EM}, $CD44^+CD62L^-$) in PBMCs, spleen, and TDLNs. These analyses revealed a significant expansion of these memory T cell subsets in mice treated with the combination therapy, particularly in the group receiving ^{PEG}HY@Ca/K-MOF in conjunction with light irradiation (Fig. 8J−O and Supporting Information Figs. S51−S53). This indicated that the synergistic strategy of light combined with ^{PEG}HY@Ca/K-MOF has a strong anti-tumor immune memory effect, which can effectively prevent tumor recurrence and metastasis. Taken together, the results presented above suggest that ^{PEG}HY@Ca/K-MOF, when activated by light exposure, induces a light-controlled mitochondrial Ca^{2+} overload-pyroptosis immunotherapy that reverses TME from immunosuppressive to immunologically favorable. This reversal triggers a robust systemic immune response and generates long-lasting immune memory.

4. Conclusions

In this work, an acid-sensitive/calcium overload elicitor was initially developed by doping calcium ions into the γ-CD-MOF framework. Subsequently, the photosensitizer HY was encapsulated within the pores of doped MOFs to constitute an effective inducer of pyroptosis-tumor metalloimmunotherapy. Finally, the PEG-modified outer layer of this formulation increased MOF stability and extended blood circulation, hence boosting tumor enrichment. The PEGylated bimetallic MOF, loaded with the phototoxic agent HY, features a relatively small size, good stability under physiological conditions, high $^1O_2$ production, effective induction of mitochondrial calcium overload capacity, and passive targeting capability to the tumor site. Benefiting from these merits, ^{PEG}HY@Ca/K-MOF exhibits superior tumor accumulation and *in vivo* photodynamic properties. Upon internalization by tumor cells, the Ca^{2+} and HY benefactors of ^{PEG}HY@Ca/K-MOF were efficiently released under weakly acidic circumstances and through photodynamic regulation, thereby disrupting the Ca^{2+} ion homeostasis and surging ROS levels within tumor cells. The light-controlled influx of mitochondrial Ca^{2+} promoted a cascade pathway that included the degradation of MICU1 protein, the generation of ROS, mitochondrial damage, and mitochondrial Ca^{2+} overload, ultimately inducing the onset of pyroptosis. Through leveraging calcium overload stress and photo-activated pyroptosis in tumor cells, ^{PEG}HY@Ca/K-MOF effectively elicited a robust ICD effect, achieving an effective suppression of primary and distant tumors under the condition of 590 nm light irradiation. More importantly, the ^{PEG}HY@Ca/K-MOF plus light group exhibited the highest frequency of T-cell infiltration, mature DCs, and memory cells, as well as the lowest percentages of immunosuppressive T_{reg} cells. Therefore, this photo-controlled mitochondrial Ca^{2+} overload-pyroptosis immunotherapy, which leverages the biocompatible and well-defined calcium-doped MOF loaded with the photosensitizer HY to induce mitochondrial calcium overload *via* MICU1 down-regulation, emerges as a novel and highly efficient synergistic strategy for melanoma treatment and holds promise as a potent immuno-adjuvant.

Acknowledgments

This study was financially supported by the Centrally Guided Local Science and Technology Development Project (No. 2024ZYD0043, China), the Chongqing Natural Science Foundation (No. CSTB2022NSCQ-MSX0350, China), the National Natural Science Foundation of China (No. 82405161), the Sichuan Province Joint Fund for Science and Education (No. 2024NSFSC2124, China), the Xinglin Scholar Research Promotion Project of Chengdu University of TCM (Nos. BSZ2024002 and QJRC2024018, China). We also wish to thank Jiayi Sun and Chen Sun from Chengdu University of TCM for their help in providing CLSM and flow cytometric facilities.

Author contributions

Qian Jing: Writing-original draft, Methodology, Data curation, Formal analysis. Mengnan Zhao: Writing-original draft, Methodology, Investigation. Yan Tang: Investigation. Tao Chen: Investigation. Mingyan Sun: Investigation. Dandan Mi: Investigation. Lan Zou: Investigation. Rujing Wang: Investigation. Jun Lu: Supervision, Writing-review & editing. Sanjun Shi: Conceptualization, Data curation, Formal analysis, Supervision, Writing-review & editing, Project administration. All of the authors have read and approved the final manuscript.

Conflicts of interest

The authors have no conflicts of interest to declare.

Appendix A. Supporting information

Supporting information to this article can be found online at https://doi.org/10.1016/j.apsb.2025.10.046.

References

1. Wang Z, Chen J, Gao R, Jiang L, Zhang G, Zhao Y, et al. Spatiotemporal manipulation metal−organic frameworks as oral drug delivery systems for precision medicine. *Coord Chem Rev* 2024;**502**: 215615.
2. Li Y, Ren HX, Chi CY, Miao YB. Artificial intelligence-guided gut−microenvironment-triggered imaging sensor reveals potential indicators of Parkinson's disease. *Adv Sci* 2024;**11**:e2307819.
3. Ma P, Wang G, Men K, Li C, Gao N, Li L. Advances in clinical application of nanoparticle-based therapy for cancer treatment: a systematic review. *Nano TransMed* 2024;**3**:100036.
4. Smaldone RA, Forgan RS, Furukawa H, Gassensmith JJ, Slawin AMZ, Yaghi OM, et al. Metal−organic frameworks from edible natural products. *Angew Chem Int Ed Engl* 2010;**49**: 8630−4.
5. Roy I, Stoddart JF. Cyclodextrin metal−organic frameworks and their applications. *Acc Chem Res* 2021;**54**:1440−53.
6. Kumar S, Jain S, Nehra M, Dilbaghi N, Marrazza G, Kim K-H. Green synthesis of metal−organic frameworks: a state-of-the-art review of potential environmental and medical applications. *Coord Chem Rev* 2020;**420**:213407.
7. Xu Y, Rashwan AK, Osman AI, Abd El-Monaem EM, Elgarahy AM, Eltaweil AS, et al. Synthesis and potential applications of cyclodextrin-based metal−organic frameworks: a review. *Environ Chem Lett* 2022;**21**:447−77.
8. Tian B, Liu J. Cyclodextrin-metal-organic frameworks in molecular delivery, detection, separation, and capture: an updated critical review. *Carbohydr Polym* 2023;**306**:120598.
9. Bieniek A, Terzyk AP, Wiśniewski M, Roszek K, Kowalczyk P, Sarkisov L, et al. MOF materials as therapeutic agents, drug carriers, imaging agents and biosensors in cancer biomedicine: recent advances and perspectives. *Prog Mater Sci* 2021;**117**:100743.
10. Wen T, Quan G, Niu B, Zhou Y, Zhao Y, Lu C, et al. Versatile nanoscale metal−organic frameworks (nMOFs): an emerging 3D nanoplatform for drug delivery and therapeutic applications. *Small* 2021;**17**:e2005064.
11. Zeng Y, Xu G, Kong X, Ye G, Guo J, Lu C, et al. Recent advances of the core−shell MOFs in tumour therapy. *Int J Pharm* 2022;**627**: 122228.
12. Gao R, Xu T, Wang Z, Ren HX, Zhang G, Zhao Y, et al. Charting a path to tumor therapy: mastery of luminescent metal−organic frameworks for precise spatiotemporal control. *Adv Funct Mater* 2024;**34**:2407535.
13. Si Y, Luo H, Zhang P, Zhang C, Li J, Jiang P, et al. CD-MOFs: from preparation to drug delivery and therapeutic application. *Carbohydr Polym* 2024;**323**:121424.
14. Woeppel KM, Zheng XS, Schulte ZM, Rosi NL, Cui XT. Nanoparticle doped PEDOT for enhanced electrode coatings and drug delivery. *Adv Healthcare Mater* 2019;**8**:e1900622.
15. Chen F, Huang P, Zhu YJ, Wu J, Zhang CL, Cui DX. The photoluminescence, drug delivery and imaging properties of multifunctional Eu3+/Gd3+ dual-doped hydroxyapatite nanorods. *Biomaterials* 2011; **32**:9031−9.
16. Zhang M, Song R, Liu Y, Yi Z, Meng X, Zhang J, et al. Calcium-overload-mediated tumor therapy by calcium peroxide nanoparticles. *Chemistry* 2019;**5**:2171−82.
17. Liu Y, Zhang M, Bu W. Bioactive nanomaterials for ion-interference therapy. *View* 2020;**1**:e18.
18. Bagur R, Hajnóczky G. Intracellular Ca^{2+} sensing: its role in calcium homeostasis and signaling. *Mol Cell* 2017;**66**:780−8.
19. Hempel N, Trebak M. Crosstalk between calcium and reactive oxygen species signaling in cancer. *Cell Calcium* 2017;**63**:70−96.
20. Liu B, Li H, Xu X, Li X, Lv N, Singh V, et al. Optimized synthesis and crystalline stability of γ-cyclodextrin metal-organic frameworks for drug adsorption. *Int J Pharm* 2016;**514**:212−9.
21. Kresse G, Furthmüller J. Efficiency of ab-initio total energy calculations for metals and semiconductors using a plane-wave basis set. *Comput Mater Sci* 1996;**6**:15−50.
22. Perdew J, Burke K, Ernzerhof M. Generalized gradient approximation made simple. *Phys Rev Lett* 1996;**77**:3865−8.
23. Blöchl PE. Projector augmented-wave method. *Phys Rev B Condens Matter* 1994;**50**:17953−79.
24. Grimme S. Semiempirical GGA-type density functional constructed with a long-range dispersion correction. *J Comput Chem* 2006;**27**: 1787−99.
25. Hu Z, Li S, Wang S, Zhang B, Huang Q. Encapsulation of menthol into cyclodextrin metal−organic frameworks: preparation, structure characterization and evaluation of complexing capacity. *Food Chem* 2021;**338**:127839.
26. Chen H, Chen Z, Zhao G, Zhang Z, Xu C, Liu Y, et al. Enhanced adsorption of U(VI) and ^{241}Am(III) from wastewater using Ca/Al layered double hydroxide@carbon nanotube composites. *J Hazard Mater* 2018;**347**:67−77.
27. Tan J, Ren H, Zhao Z, Xin X, Shi Y, Yang D, et al. Ca^{2+} doped metal organic frameworks for enhanced photocatalytic ammonia synthesis. *Chem Eng J* 2023;**466**:143259.
28. Zhang H, Zhang X, Wang X, Sun Q, Liu H, Ji H, et al. Activity promotion of Rh_1Ca_x/Al_2O_3 single-atom catalyst in 1-octene hydroformylation: a volcano curve exists between Ca adding ratio and catalytic activity. *Sci China Chem* 2024;**67**:1187−92.
29. Lin Z, Huang H, Cheng L, Hu W, Xu P, Yang Y, et al. Tuning the p-orbital electron structure of s-block metal Ca enables a high-performance electrocatalyst for oxygen reduction. *Adv Mater* 2021;**33**: e2107103.
30. Li J, Liu P, Chen Y, Zhou J, Li J, Yang J, et al. A customized hydrophobic porous shell for MOF-5. *J Am Chem Soc* 2023;**145**: 19707−14.
31. Zhang L, Feng J, Wu L, Ma X, Song X, Jia S, et al. Oxophilicity-controlled CO_2 electroreduction to C_{2+} alcohols over lewis acid metal-doped $Cu^{\delta+}$ catalysts. *J Am Chem Soc* 2023;**145**:21945−54.
32. Wang L, Wang T, Zhang Y, Kang X, Ouyang Xk, Yu X, et al. Biomimetic nanosystems harnessing NIR-II photothermal effect and hypoxia-responsive prodrug for self-amplifying and synergistic tumor treatment. *Nano Today* 2024;**57**:102395.
33. Kritskiy I, Volkova T, Surov A, Terekhova I. γ-Cyclodextrin-metal organic frameworks as efficient microcontainers for encapsulation of leflunomide and acceleration of its transformation into teriflunomide. *Carbohydr Polym* 2019;**216**:224−30.
34. Dayyih AA, Gutberlet B, Preis E, Engelhardt KH, Amin MU, Abdelsalam AM, et al. Thermoresponsive liposomes for photo-triggered release of hypericin cyclodextrin inclusion complex for efficient antimicrobial photodynamic therapy. *ACS Appl Mater Interfaces* 2022;**14**:31525−40.
35. Gusmão LA, Machado AEH, Perussi JR. Improved hypericin solubility *via* β-cyclodextrin complexation: photochemical and theoretical study for PDT applications. *Photodiagnosis Photodyn Ther* 2022;**40**: 103073.
36. Min T, Lei Y, Cheng C, Luo Y, Zhang Y, Yue J. Highly efficient anchoring of γ-cyclodextrin-MOFs on chitosan/cellulose film by *in situ* growth to enhance encapsulation and controlled release of carvacrol. *Food Hydrocoll* 2024;**150**:109633.
37. Du J, Jia T, Li F, Li Y, Wang Q, He L, et al. MOF-coated upconversion nanoparticle agents enable synergistic photodynamic therapy and immunotherapy. *Adv Funct Mater* 2024;**34**:2401272.

38. Lu S, Shi Z, Ding C, Wang W, Zhang W, Huang L, et al. BRD4-targeted photodegradation nanoplatform for light activatable melanoma therapy. *Biomaterials* 2025;**317**:123101.
39. Nosaka Y, Nosaka AY. Generation and detection of reactive oxygen species in photocatalysis. *Chem Rev* 2017;**117**:11302−36.
40. Li G, Li P, Jiang Q, Zhang Q, Qiu J, Li D, et al. Discovery of a pyridophenoselenazinium-based photosensitizer with high photodynamic efficacy against breast cancer cells. *Acta Mater Med* 2023;**2**: 96−105.
41. Li J, Mi D, Wang R, Li Y, Zhao M, Shi S. A lava-inspired proteolytic enzyme therapy on cancer with a PEG-based hydrogel enhances tumor distribution and penetration of liposomes. *J Nanobiotechnol* 2024;**22**: 216.
42. Mi D, Li J, Wang R, Li Y, Zou L, Sun C, et al. Postsurgical wound management and prevention of triple-negative breast cancer recurrence with a pryoptosis-inducing, photopolymerizable hydrogel. *J Control Release* 2023;**356**:205−18.
43. Wang R, Zou L, Yi Z, Zhang Z, Zhao M, Shi S. PLGA nanoparticles loaded with curcumin produced luminescence for cell bioimaging. *Int J Pharm* 2023;**639**:122944.
44. Roderick HL, Cook SJ. Ca^{2+} signalling checkpoints in cancer: remodelling Ca^{2+} for cancer cell proliferation and survival. *Nat Rev Cancer* 2008;**8**:361−75.
45. Görlach A, Bertram K, Hudecova S, Krizanova O. Calcium and ROS: a mutual interplay. *Redox Biol* 2015;**6**:260−71.
46. Madreiter-Sokolowski CT, Thomas C, Ristow M. Interrelation between ROS and Ca^{2+} in aging and age-related diseases. *Redox Biol* 2020;**36**:101678.
47. Ravi B, Foyer CH, Pandey GK. The integration of reactive oxygen species (ROS) and calcium signalling in abiotic stress responses. *Plant Cell Environ* 2023;**46**:1985−2006.
48. Bertero E, Maack C. Calcium signaling and reactive oxygen species in mitochondria. *Circ Res* 2018;**122**:1460−78.
49. Giorgi C, Marchi S, Pinton P. The machineries, regulation and cellular functions of mitochondrial calcium. *Nat Rev Mol Cell Biol* 2018;**19**: 713−30.
50. Walkon LL, Strubbe-Rivera JO, Bazil JN. Calcium overload and mitochondrial metabolism. *Biomolecules* 2022;**12**:1891.
51. Smith MA, Schnellmann RG. Calpains, mitochondria, and apoptosis. *Cardiovasc Res* 2012;**96**:32−7.
52. Cui C, Merritt R, Fu L, Pan Z. Targeting calcium signaling in cancer therapy. *Acta Pharm Sin B* 2017;**7**:3−17.
53. Pászty K, Verma AK, Padányi R, Filoteo AG, Penniston JT, Enyedi Á. Plasma membrane Ca^{2+} ATPase isoform 4b is cleaved and activated by Caspase-3 during the early phase of apoptosis. *J Biol Chem* 2002; **277**:6822−9.
54. Marchi S, Giorgi C, Galluzzi L, Pinton P. Ca^{2+} fluxes and cancer. *Mol Cell* 2020;**78**:1055−69.
55. Monteith GR, Prevarskaya N, Roberts-Thomson SJ. The calcium−cancer signalling nexus. *Nat Rev Cancer* 2017;**17**: 367−80.
56. Zheng S, Wang X, Zhao D, Liu H, Hu Y. Calcium homeostasis and cancer: insights from endoplasmic reticulum-centered organelle communications. *Trends Cell Biol* 2023;**33**:312−23.
57. Garbincius JF, Elrod JW. Mitochondrial calcium exchange in physiology and disease. *Physiol Rev* 2022;**102**:893−992.
58. Chakraborty PK, Mustafi SB, Xiong X, Dwivedi SKD, Nesin V, Saha S, et al. MICU1 drives glycolysis and chemoresistance in ovarian cancer. *Nat Commun* 2017;**8**:14634.
59. Csordás G, Golenár T, Seifert Erin L, Kamer Kimberli J, Sancak Y, Perocchi F, et al. MICU1 controls both the threshold and cooperative activation of the mitochondrial Ca^{2+} uniporter. *Cell Metab* 2013;**17**: 976−87.
60. Kamer KJ, Mootha VK. The molecular era of the mitochondrial calcium uniporter. *Nat Rev Mol Cell Biol* 2015;**16**:545−53.
61. Liu JC, Liu J, Holmström KM, Menazza S, Parks RJ, Fergusson MM, et al. MICU1 serves as a molecular gatekeeper to prevent *in vivo* mitochondrial calcium overload. *Cell Rep* 2016;**16**:1561−73.
62. Mallilankaraman K, Doonan P, Cárdenas C, Chandramoorthy Harish C, Müller M, Miller R, et al. MICU1 is an essential gatekeeper for MCU-mediated mitochondrial Ca^{2+} uptake that regulates cell survival. *Cell* 2012;**151**:630−44.
63. Pendin D, Greotti E, Pozzan T. The elusive importance of being a mitochondrial Ca^{2+} uniporter. *Cell Calcium* 2014;**55**:139−45.
64. Lan T, Zhang K, Lin F, He Q, Wu S, Xu Z, et al. Effects of MICU1-Mediated mitochondrial calcium uptake on energy metabolism and quality of vitrified-thawed mouse metaphase II oocytes. *Int J Mol Sci* 2022;**23**:8629.
65. Kon N, Murakoshi M, Isobe A, Kagechika K, Miyoshi N, Nagayama T. DS16570511 is a small-molecule inhibitor of the mitochondrial calcium uniporter. *Cell Death Discov* 2017;**3**:17045.
66. Loveless R, Bloomquist R, Teng Y. Pyroptosis at the forefront of anticancer immunity. *J Exp Clin Cancer Res* 2021;**40**:264.
67. Li M, Kim J, Rha H, Son S, Levine MS, Xu Y, et al. Photon-controlled pyroptosis activation (photopyro): an emerging trigger for antitumor immune response. *J Am Chem Soc* 2023;**145**:6007−23.
68. Krishnaswami V, Mohanan DP, Raja SAJ, Natarajan B, Velusamy S. Nanotechnology-based advancements for effective delivery of phytoconstituents for ocular diseases. *Nano TransMed* 2024;**3**:100056.
69. Li X, Wang H, Chen Y, Li Z, Liu S, Guan W, et al. Novel emerging nano-assisted anti-cancer strategies based on the STING pathway. *Acta Mater Med* 2023;**2**:323−41.
70. Zeng W, Li Z, Huang Q, Ding C, Yang L, Wang W, et al. Multifunctional mesoporous polydopamine-based systematic delivery of STING agonist for enhanced synergistic photothermal-immunotherapy. *Adv Funct Mater* 2023;**34**:2307241.
71. Zhang Y, Yu X, Luo L, Xu Y, Zhang H, Mao Z, et al. Engineered manganese-BODIPY coordinated nanoadjuvants for enhanced NIR-II photo-metalloimmunotherapy. *J Control Release* 2024;**376**:1115−29.
72. Fei Z, Fan Q, Dai H, Zhou X, Xu J, Ma Q, et al. Physiologically triggered injectable red blood cell-based gel for tumor photoablation and enhanced cancer immunotherapy. *Biomaterials* 2021;**271**:120724.